J. Phys.: Condens. Matter **21** (2009) 185002 (22pp) doi:10.1088/0953-8984/21/18/185002

On the transition from boundary lubrication to hydrodynamic lubrication in soft contacts

B N J Persson[1] **and M Scaraggi**[1,2]

[1] IFF, FZ-Jülich, D-52425 Jülich, Germany
[2] DIMeG-Politecnico di Bari, V.le Japigia 182, I-70126 Bari, Italy

Received 3 November 2008, in final form 18 January 2009
Published 11 March 2009
Online at stacks.iop.org/JPhysCM/21/185002

Abstract
We consider the contact between elastically soft solids with randomly rough surfaces in sliding contact in a fluid, which is assumed to be Newtonian with constant (pressure-independent) viscosity. We discuss the nature of the transition from boundary lubrication at low sliding velocity, where direct solid–solid contact occurs, to hydrodynamic lubrication at high sliding velocity, where the solids are separated by a thin fluid film. We consider both hydrophilic and hydrophobic systems, and cylinder-on-flat and sphere-on-flat sliding configurations. We show that, for elastically soft solids such as rubber, including cavitation or not results in nearly the same friction.

(Some figures in this article are in colour only in the electronic version)

1. Introduction

At present, there is no theory which can accurately describe the transition from boundary lubrication to hydrodynamic lubrication for elastic solids with randomly rough surfaces [1, 2]. The main problem in modeling real contacts is that most surfaces of practical interest have surface roughness over a large range of length scales, typically from cm to nm, which results in too many degrees of freedom to be (actually) handled by numerical methods, such as the finite element or finite difference method [3, 4]. Many attempts were made in order to overcome this computational problem, by mean of spatial averaging [5–8] or small perturbation techniques [9–11]. Basically, the surface roughness is effectively removed (integrated out), resulting in effective equations of motion for fluid flow between elastic solids with smooth surfaces with the (macroscopic) shape or curvature of the solid objects under study.

Patir and Cheng (P&C) [5, 6] were the first to adopt the concept of flow factors into an averaged Reynolds equation. The flow factors are determined by solving the fluid flow equation for a small (rectangular) interfacial unit of the rough surfaces. The flow factors are obtained by averaging over several realizations of the rough surfaces. The basic assumption in this approach is that the surface roughness occur at length scales much shorter than the macroscopic radius of curvatures of the solid objects. In this case the flow factors will determine the influence of the surface roughness on the (average) fluid flow in the macroscopic junction. However, in this approach the local elastic deformation resulting from the asperity–asperity (and asperity–fluid) interaction is neglected (but the macroscopic elastic deformations, e.g. the Hertzian-like deformation of an elastic ball in contact with a flat, is of course included), which makes the P&C method incompatible with any dry contact mechanics theory (to be used in conjunction with the averaged fluid equation).

Another interesting approach is based on the application of homogenization techniques to the fluid equation, see [10]. As for the P&C approach, this approach does not consider the local elastic deformations resulting from the asperity–asperity and asperity–fluid interactions and therefore cannot accurately describe mixed lubrication.

Here we will study the influence of surface roughness on the nature of the transition between boundary lubrication and hydrodynamic lubrication for soft contacts. In general, one needs to distinguish between hydrophobic and hydrophilic systems. Let us introduce the spreading pressure (a line pressure) [12]

$$S = \gamma_{S_1S_2} - \gamma_{S_1L} - \gamma_{S_2L}, \tag{1}$$

where γ_{S_1L} is the interfacial energy (per unit area) between solid **1** and the liquid, and similar for γ_{S_2L}, and where $\gamma_{S_1S_2}$ is the solid **1**—solid **2** interfacial energy per unit area. When

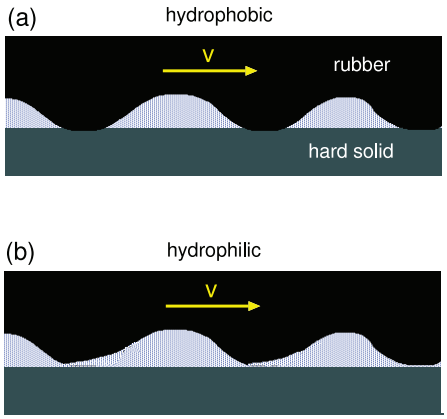

Figure 1. Asperity contact for (a) hydrophobic surfaces and (b) hydrophilic surfaces. For hydrophilic surfaces, most of the asperity contact regions are separated by thin fluid layers (schematic).

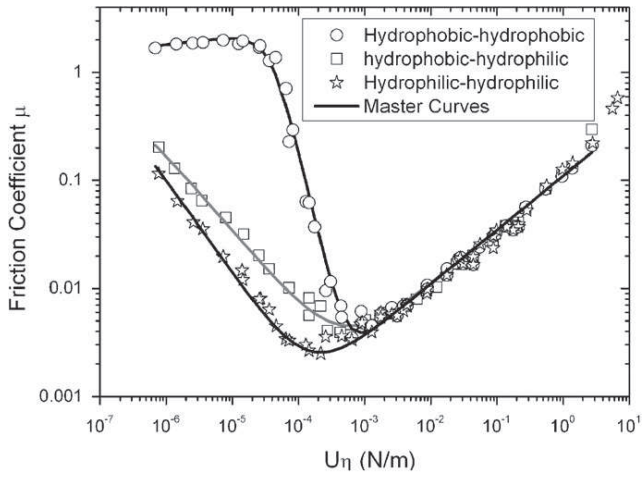

Figure 2. Friction coefficient for silicon rubber sliding on hard substrate surfaces. For hydrophilic and hydrophobic surfaces. Reproduced from [32]. Copyright 2007 with permission from Elsevier.

$S < 0$ (hydrophobic surfaces), a dewetting transition may occur in the asperity contact regions (dry asperity contact) [13–15], while for $S > 0$ (hydrophilic surfaces), the asperity contact regions tend to be separated by thin fluid layers as illustrated in figure 1. Qualitatively, we may state that a short-ranged fluid-mediated attraction or repulsion occurs between the solid walls depending on if $S < 0$ or $S > 0$, respectively. In the mixed lubrication region this will typically result in a lower sliding friction for the hydrophilic system as compared to the hydrophobic system, in qualitative agreement with experimental data, see figure 2.

In sections 2 and 3 we study the stationary sliding of an elastic cylinder and a ball on a flat rigid substrate by neglecting the fluid–asperity interaction, which may be a good approximation for hydrophobic systems, where the asperity contact regions may, at low enough sliding velocity, be dry due to dewetting transitions. In section 4 we will study the effect of the fluid–asperity interaction for an elastic nominally flat surface sliding on a flat rigid substrate. In section 5 we discuss the theory and in section 6 we present results for wiper blades and tires. The fluid is assumed Newtonian, incompressible and isoviscous. The cylinder and the ball have isotropic surface roughness on many different length scales, which we include in the analysis using a recently developed contact mechanics theory [18–23]. One interesting result is that for elastically soft solids such as rubber, including cavitation in the analysis results in nearly the same result as when cavitation is absent, i.e. the solution is insensitive to the exact boundary conditions used when solving the fluid flow equations.

2. Cylinder on flat

We consider first the simplest problem of an elastic cylinder (length L, radius R, Young's elastic modulus E and Poisson ratio ν) with a rough surface sliding on a rigid solid with a perfectly flat surface. We assume $L \gg R$ and that the sliding occurs in the direction perpendicular to the cylinder axis. We introduce a coordinate system with the x axis along the sliding direction and with $x = 0$ on the cylinder axis, see figure 3.

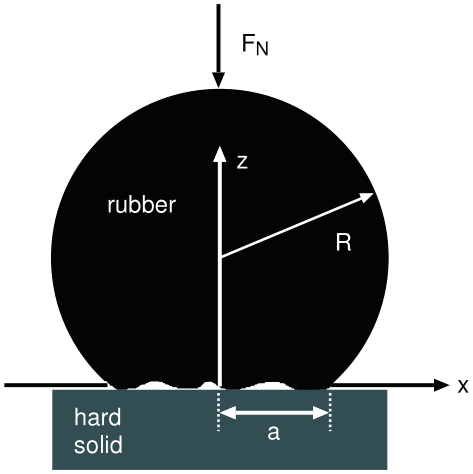

Figure 3. A rubber cylinder (or ball) with a rough surface in squeeze-contact with a flat hard substrate (schematic).

The cylinder is squeezed against the substrate by the normal force F_N (see figure 3), and in the contact region between the cylinder and the substrate a nominal (locally averaged) pressure occurs:

$$p_0(x) = p_{\rm cont}(x) + p_{\rm fluid}(x), \tag{2}$$

where $p_{\rm cont}$ is the pressure due to the direct solid–solid interaction and $p_{\rm fluid}$ is the fluid pressure. Here and in what follows we measure the pressure relative to the atmospheric pressure. We consider a stationary case so that

$$\int_{-\infty}^{\infty} {\rm d}x\ p_0(x) = \frac{F_N}{L}. \tag{3}$$

We have [19, 23]

$$p_{\rm cont} \approx \beta E^* \exp\left(-\alpha \frac{\bar{u}(x)}{h_{\rm rms}}\right), \tag{4}$$

where $\bar{u}(x)$ is the nominal separation between the surfaces and where the effective elastic modulus $E^* = E/(1-\nu^2)$ (E is the Young's elastic modulus and ν the Poisson ratio). Equation (4) is valid for large enough $\bar{u}$ (typically $\bar{u} > h_{\rm rms}$). Since an infinite high pressure is necessary in order to squeeze the solids into complete contact we must have $p_{\rm cont} \to \infty$ as $\bar{u} \to 0$. This is, of course, not obeyed by (4), and in our calculations we use the numerically calculated relation (see [19, 23]) $p_{\rm cont}(\bar{u})$, which reduces to (4) for large enough $\bar{u}$. However, in the present applications the contact area is rather small, and using (4) gives nearly the same result as for the numerically calculated relation. We also note that, in the present case, where we have assumed that the spreading pressure $S < 0$, there is an effective short-ranged attraction between the surfaces which may modify the relation between $p_{\rm cont}$ and $\bar{u}$ somewhat (see [24]), but we will assume that this effect is small in the present case.

The fluid flow is determined by [25]

$$\frac{{\rm d}p_{\rm fluid}}{{\rm d}x} = 6\eta v_0 \left(\frac{1}{\bar{u}^2(x)} - \frac{u^*}{\bar{u}^3(x)}\right). \tag{5}$$

where η is the fluid viscosity and v_0 the sliding velocity. u^* is a constant determined below. We will first assume that cavitation occurs on the exit side of the fluid flow region between the cylinder and the substrate. This is taken into account by using the boundary conditions $p = 0$ (note: we measure pressure relative to the external or atmospheric pressure) and ${\rm d}p/{\rm d}x = 0$ for $x = x_1$ (see appendix A). In addition we assume that $p(x) \to 0$ as $x \to -\infty$. Integrating (5) gives

$$p_{\rm fluid}(x) = 6\eta v_0 \int_{-\infty}^{x} {\rm d}x' \left(\frac{1}{\bar{u}^2(x')} - \frac{u^*}{\bar{u}^3(x')}\right). \tag{6}$$

We now study the integral in (6) as a function of x. For large negative x, the integral is positive and with increasing x it increases and then, if u^* is large enough, decreases until $p_{\rm fluid}(x) = 0$ for $x = x_1$. Note that the condition ${\rm d}p/{\rm d}x = 0$ for $x = x_1$ implies that $u^* = \bar{u}(x_1)$. The elastic deformation field [25]

$$\bar{u}(x) = u_0 + \frac{x^2}{2R} - \frac{2}{\pi E^*}\int_{-\infty}^{\infty} {\rm d}x'\, p_0(x') \ln\left|\frac{x-x'}{x'}\right|. \tag{7}$$

In addition the pressure $p_0(x)$ must satisfy the normalization condition (3). Equations (2), (3), (4), (6) and (7) represent five equations for the five unknown variables p_0, $p_{\rm cont}$, $p_{\rm fluid}$, $\bar{u}$ and u_0. In the theory presented above, cavitation is assumed to occur only on the macroscopic scale.

It is convenient to introduce dimensionless quantities. Let us measure distance (x and $\bar{u}$) in units of R and pressure in units of E^*. In this case the equations above take the form

$$p_0(x) = p_{\rm cont}(x) + p_{\rm fluid}(x), \tag{8}$$

$$p_{\rm cont} \approx \beta \exp\left(-\alpha \bar{u}(x)\frac{R}{h_{\rm rms}}\right), \tag{9}$$

$$p_{\rm fluid}(x) = 6\frac{\eta v_0}{RE^*}\int_{-\infty}^{x} {\rm d}x' \left(\frac{1}{\bar{u}^2(x')} - \frac{u^*}{\bar{u}^3(x')}\right), \tag{10}$$

$$\bar{u}(x) = u_0 + \frac{x^2}{2} - \frac{2}{\pi}\int_{-\infty}^{\infty} {\rm d}x'\, p_0(x') \ln\left|\frac{x-x'}{x'}\right|, \tag{11}$$

$$\int_{-\infty}^{\infty} {\rm d}x'\, p_0(x') = \frac{F_{\rm N}}{RLE^*}. \tag{12}$$

Thus, the problem depends only on three dimensionless parameters, namely $h_{\rm rms}/R$, $\eta v_0/RE^*$ and $F_{\rm N}/RLE^*$, and on the parameters α and β which are determined by the surface roughness power spectrum $C(q)$.

The frictional stress is given by

$$\sigma_{\rm f} = \sigma_{\rm cont} + \sigma_{\rm fluid}. \tag{13}$$

The (nominal) frictional stress resulting from the area of solid–solid contact is

$$\sigma_{\rm cont} = \sigma_1 \frac{A_1}{A_0},$$

where $A_1 = A(\zeta_1)$ is the area of real contact at the highest magnification and A_0 is the nominal contact area. In the present calculations we have neglected the adhesion between the solids but, as pointed out before, when the spreading pressure $S < 0$ there will be an effective short-ranged attraction between the surfaces, which (at low sliding velocity) will tend to increase the contact area A_1. This effect can be taken into account in our formalism [21], but we neglect it here for simplicity. The shears stress σ_1 is assumed to be independent of the local pressure, which is likely to be a good approximation for elastically soft materials such as rubber. We also assume that σ_1 is independent of the sliding velocity, but experiments on silicon rubber sliding on flat dry surfaces have shown that this is not always a good approximation [26]. As long as $A_1/A_0 \ll 1$, which prevails in the applications presented below, we have $A_1/A_0 = \chi p_{\rm cont}/E^*$, where χ depends only on the surface roughness power spectrum $C(q)$, so that [18]

$$\sigma_{\rm cont}(x) \approx \chi \sigma_1 p_{\rm cont}(x)/E^*. \tag{14}$$

The frictional shear stress from the fluid

$$\sigma_{\rm fluid} = \eta \frac{\partial v_x}{\partial z}. \tag{15}$$

Since the velocity profile

$$v_x(x,z) = v_0 \frac{z}{\bar{u}(x)} + v_1(x)\frac{z}{\bar{u}(x)}\left(1 - \frac{z}{\bar{u}(x)}\right),$$

where

$$v_1 = \frac{\bar{u}^2}{2\eta}\frac{\partial p_{\rm fluid}}{\partial x},$$

we get

$$\sigma_{\rm fluid} = \eta\frac{v_0}{\bar{u}(x)} \pm \frac{\bar{u}(x)}{2}\frac{\partial p_{\rm fluid}}{\partial x},$$

where the + and − signs refer to the surfaces $z = \bar{u}(x)$ and $z = 0$, respectively. Using (6) this can also be written as

$$\sigma_{\rm fluid} = \frac{\eta v_0}{\bar{u}(x)}\left[1 \pm 3\left(1 - \frac{\bar{u}(x_1)}{\bar{u}(x)}\right)\right]. \tag{16}$$

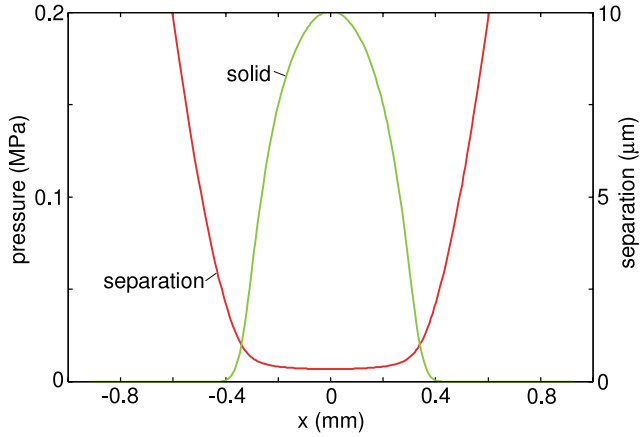

Figure 4. The contact pressure distribution and the interfacial separation between an elastic cylinder (elastic modulus $E = 10$ MPa and Poisson ratio $\nu = 0.5$) and a nominal flat substrate with the root-mean-square roughness 1 μm. The cylinder radius $R = 1$cm and the loading force per unit length $F_N/L = 100$ N m^{-1}. The half-width of the Hertz contact area (for flat substrate surface) is $a_H = 0.0309$ cm and the maximum and average Hertz contact pressure are 0.2060 MPa and 0.1618 MPa, respectively. The substrate has a self-affine fractal surface with the fractal dimension $D_f = 2.2$ and the root-mean-square roughness 1 μm and with $q_0 = 1 \times 10^4$ m^{-1} and $q_1 = 0.78 \times 10^{10}$ m^{-1}. The fluid viscosity $\eta = 0.1$ Pa s. Sliding velocity $v = 1.0 \times 10^{-5}$ m s^{-1}.

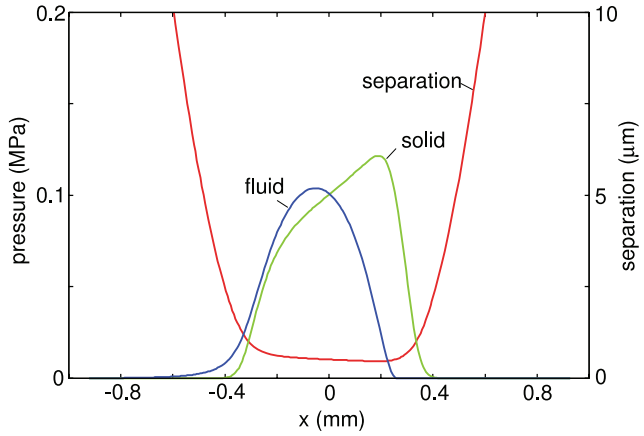

Figure 5. The same as in figure 4 but for the sliding velocity $v = 1.5 \times 10^{-3}$ m s^{-1}.

The friction coefficient[3]

$$\mu = \frac{L}{F_N}\int dx\, \sigma_f(x) = \frac{L}{F_N}\int dx\, (\sigma_{cont}(x) + \sigma_{fluid}(x))\,. \tag{17}$$

[3] We have assumed that the area of real contact between the solids is always small compared to the nominal contact area, at least in the mixed (and hydrodynamic) lubrication regime. If this is not the case the equation for the (locally averaged) fluid stress, given by equations (16) and (29), must be corrected for the fact that the fluid occupies only part of the sliding junction. In the roughest treatment of this effect one introduces on the right-hand side in (16) (and (29)) the additional factor $(1 - A(x)/A_0)^2$, where $A(x)/A_0$ is the (normalized) area of real contact (which depends on x because of the macroscopic curvature of the solids). Here one factor of $(1 - A(x)/A_0)$ takes into account the reduction in the fluid area and another factor of $(1 - A(x)/A_0)$ takes into account that the average fluid film thickness in the non-contact area is $\bar{u}/(1 - A(x)/A_0)$ rather than $\bar{u}$ (note: the frictional shear stress scales as $\sim 1/u$, where u is the surface separation).

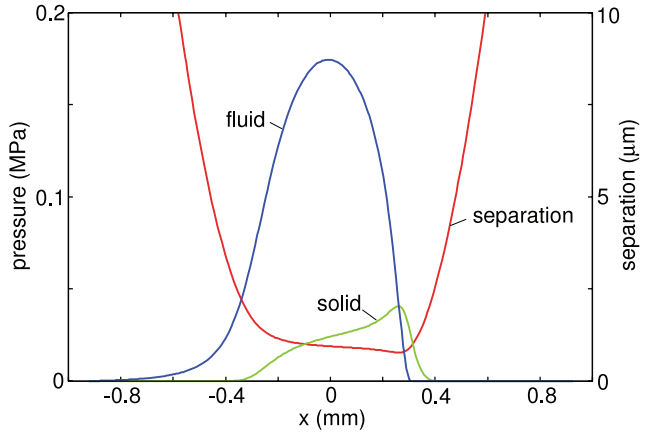

Figure 6. The same as in figure 4 but for the sliding velocity $v = 6.6 \times 10^{-3}$ m s^{-1}.

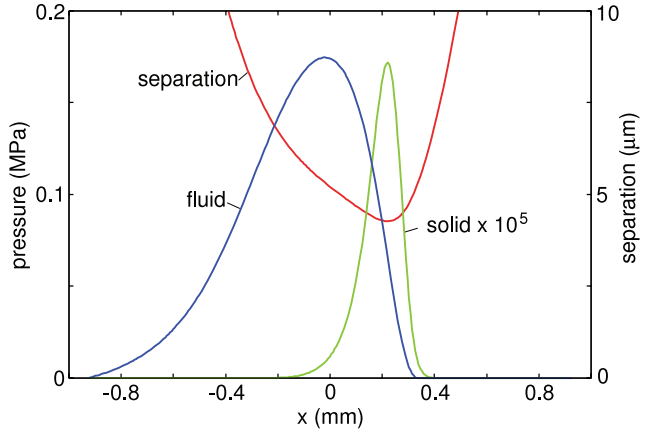

Figure 7. The same as in figure 4 but for the sliding velocity $v = 0.12$ m s^{-1}.

The equations above are conveniently solved numerically as described in appendix B. In figures 4–7 we show the solid and fluid pressure distributions (left scale) and surface separation (right scale) for increasing sliding velocities, $v = 1.0 \times 10^{-5}$, 1.5×10^{-3}, 6.6×10^{-3} and 0.12 m s^{-1}. In the calculation we have assumed the substrate to be rigid, with the root-mean-square roughness 1 μm and the fractal dimension $D_f = 2.2$. The rubber has the elastic modulus 10 MPa. Note that at the lowest sliding velocity the pressure distribution is Hertzian-like, with a small broadening resulting from the surface roughness.

Figure 8 shows the friction coefficient, μ, as a function of the product of the sliding velocity and the fluid viscosity, ηv, on a log–log scale. The calculation is for the same system as in figure 4 but for three different root-mean-square roughness values, 1, 3 and 6 μm. Figure 9 shows the friction coefficient, μ, and the relative area of real contact, A/A_0, as a function of the sliding velocity (log–log scale).

Figure 10 shows the fraction of the loading force (per unit length) carried by the fluid and by the asperity contact regions as a function of the sliding velocity (log–log scale). The vertical dashed line indicates the velocity where the friction

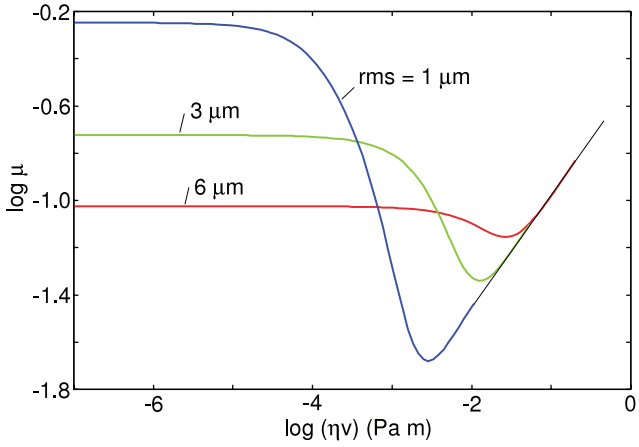

Figure 8. The friction coefficient, μ as a function of the product of the sliding velocity and the fluid viscosity, ηv, and a log–log scale. For the same system as in figure 4 but for three different root-mean-square roughness values, 1, 3 and 6 μm.

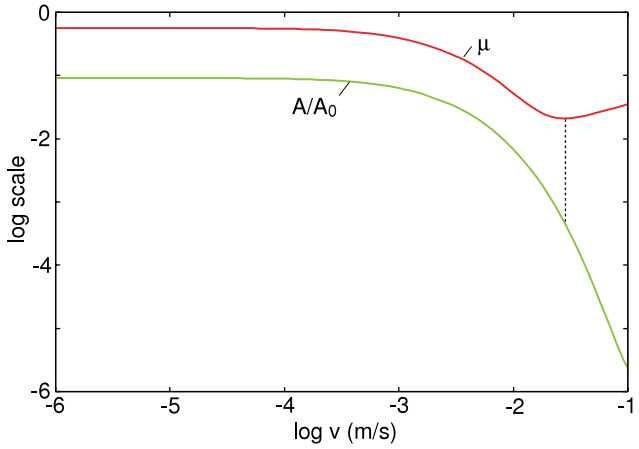

Figure 9. The friction coefficient, μ, and the relative area of real contact, A/A_0, as a function of the sliding velocity (log–log scale). For the same system as in figure 4.

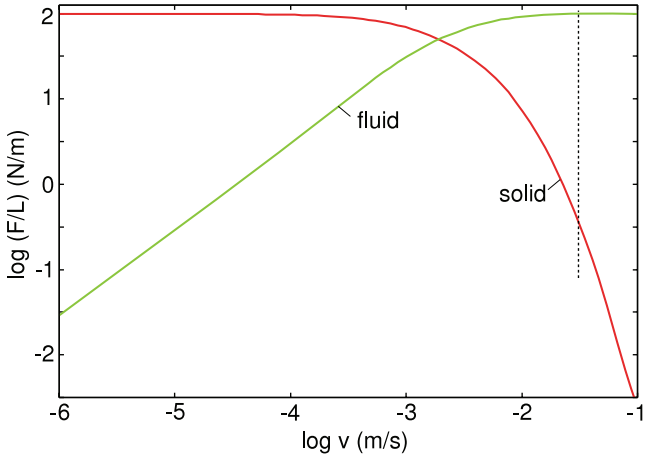

Figure 10. The load force (per unit length) carried by the fluid and the solid contact as a function of the sliding velocity (log–log scale). For the same system as in figure 4.

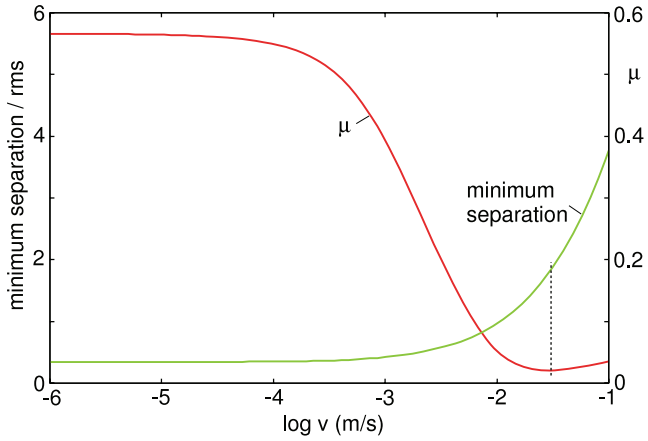

Figure 11. The friction coefficient, μ, and the minimum surface separation as a function of the logarithm of the sliding velocity. For the same system as in figure 4.

force is minimal. Note that, when the friction is minimal, the fraction of the load carried by the asperities is only ≈0.003. This result depends on the shear stress σ_1, but the value we use is typical for PDMS rubber sliding on smooth hard inert substrates [26]. Figure 11 shows the friction coefficient, μ, and the minimum surface separation as a function of the logarithm of the sliding velocity.

In figure 12 we show the friction coefficient, μ, as a function of the product ηv, assuming no cavitation (red curve) and with cavitation (green curve). It is remarkable how small an effect the cavitation has on the relation $\mu(v)$, in spite of the fact that the fluid pressure distribution, $p_{\text{fluid}}(x)$, is rather different in the two cases. This is illustrated in figure 13 for the same parameters as in figure 5, but without cavitation.

Note that, even in the absence of cavitation, the fluid pressure results in a slight tilting of the surface of the sliding object with respect to the substrate [27]. In fact, the interfacial separation is very similar with and without cavitation (compare figures 5 and 13). The average fluid film thickness, when most

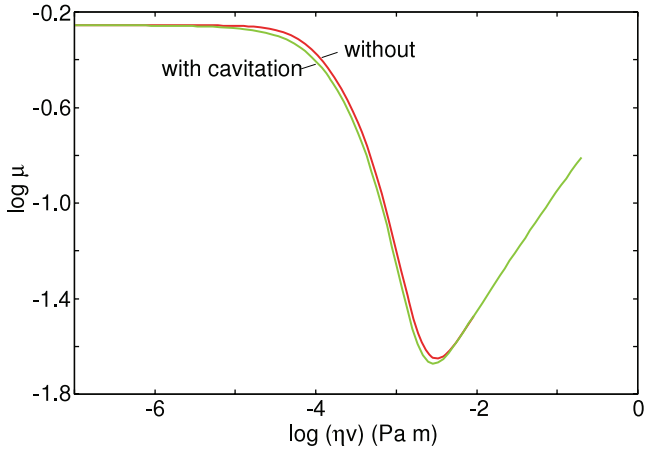

Figure 12. The friction coefficient, μ, as a function of the product ηv of the sliding velocity v and the fluid viscosity η, without cavitation (red curve) and with cavitation (green curve) (log–log scale with 10 as basis). For the same system as in figure 4.

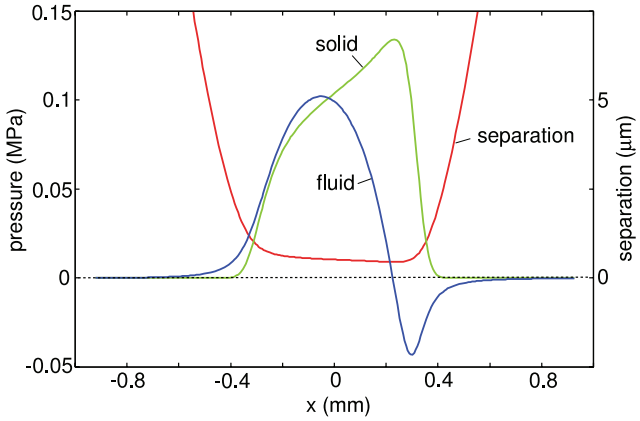

Figure 13. The same as in figure 5 (i.e. $E = 10$ MPa and $v = 1.5 \times 10^{-3}$ m s^{-1}) but without cavitation.

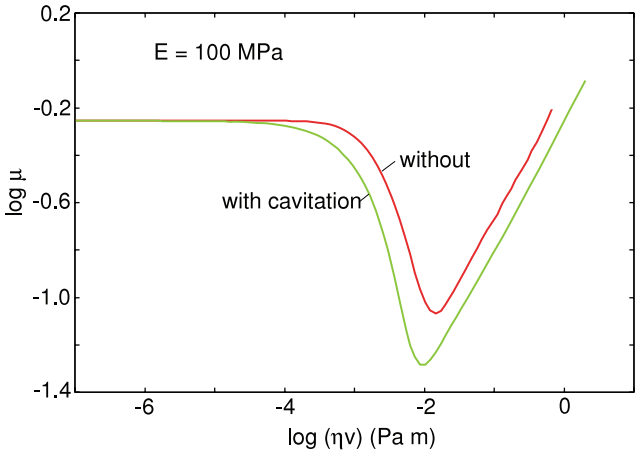

Figure 14. The friction coefficient, μ, as a function of the product ηv of the sliding velocity v and the fluid viscosity η, without cavitation (red curve) and with cavitation (green curve) (log–log scale with 10 as basis). The elastic modulus $E = 100$ MPa and frictional shear stress $\sigma_1 = 10$ MPa. The other parameters are as for the same system in figure 4.

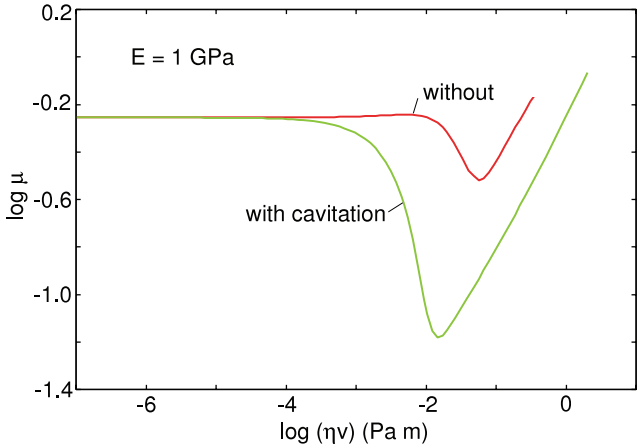

Figure 15. The friction coefficient, μ, as a function of the product ηv of the sliding velocity v and the fluid viscosity η, without cavitation (red curve) and with cavitation (green curve) (log–log scale with 10 as basis). The elastic modulus $E = 1$ GPa and frictional shear stress $\sigma_1 = 100$ MPa. The other parameters are as for the same system in figure 4.

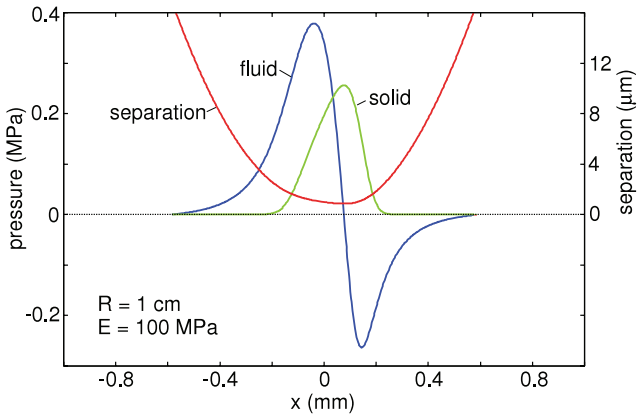

Figure 16. The same as in figure 5 but for the elastic modulus $E = 100$ MPa and the sliding velocity 0.027 m s^{-1}.

of the external load is carried by the fluid (as in figures 5–7), is well approximated by the formula $\bar{u} \approx (\kappa \eta v_0 \lambda / \bar{p})^{1/2}$ (with $\kappa \approx 0.2$), where $\bar{p}$ is the average fluid pressure in the 'contact area' (see appendix C), which is similar to the Hertz average pressure for the corresponding static contact problem.

In figures 14 and 15 we show similar results as in figure 12, but for higher elastic modulus, $E = 100$ MPa (and $\sigma_1 = 10$ MPa) and 1 GPa (and $\sigma_1 = 100$ MPa), respectively. As expected, in these cases the deviation between the results with cavitation and with no cavitation is larger than for the case where elastic modulus $E = 10$ MPa.

In figure 16 we show, for the case where no cavitation occurs, the fluid pressure, the asperity contact pressure and the interfacial separation for the case when the elastic modulus $E = 100$ MPa and the sliding velocity $v = 0.027$ m s^{-1}. The other parameters are the same as in figures 13 and 5. Similar results are shown in figure 17 for the case when the elastic modulus $E = 1$ GPa and the sliding velocity $v = 0.123$ m s^{-1}. Note that in this case the fluid pressure profile is nearly antisymmetric around the midpoint $x = 0$. For the limiting case of a rigid elastic cylinder (and rigid substrate) the hydrodynamic pressure will be antisymmetric through the mid-plane of the (symmetric) contact junction, i.e. no net load will be carried by the fluid. When cavitation is included in the calculation the fluid will (even for rigid solids) carry some fraction of the load, but not as much as for elastic solids (compare figures 12 and 15 and note that the minimal friction is smaller in the case where the solid walls can deform).

3. Sphere on flat

We consider now the problem of an elastic ball (radius R) with a rough surface sliding on a rigid perfectly flat surface. We assume sliding along the x axis (see figure 3). The ball is squeezed against the substrate by the force F_N, and in the contact region between the ball and the substrate occurs a

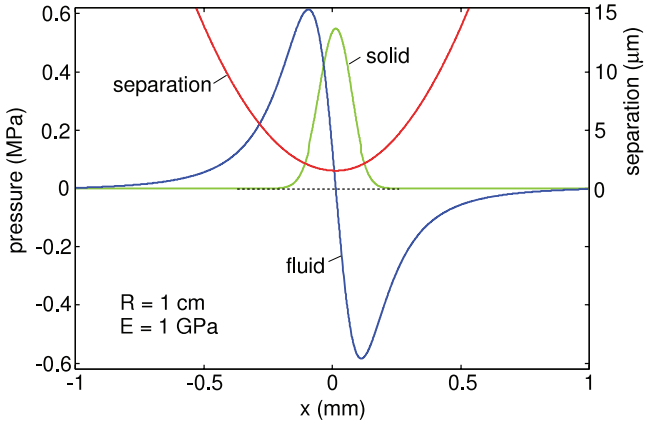

Figure 17. The same as in figure 5 but for the elastic modulus $E = 1$ GPa and the sliding velocity 0.123 m s^{-1}.

nominal pressure (locally averaged):

$$p_0(\mathbf{x}) = p_{\rm cont}(\mathbf{x}) + p_{\rm fluid}(\mathbf{x}).$$

The normal load

$$\int_{-\infty}^{\infty} {\rm d}^2x\; p_0(\mathbf{x}) = F_{\rm N}. \tag{18}$$

The contact pressure

$$p_{\rm cont}(\mathbf{x}) = p_{\rm cont}(\bar{u}(\mathbf{x})) \tag{19}$$

is defined in section 2.

The fluid flow is determined by the (isoviscous and isodense) Reynolds equation [28]:

$$\nabla\cdot\left(\bar{u}(\mathbf{x})^3\nabla p_{\rm fluid}(\mathbf{x})\right) = 6\eta v_0\frac{\partial\bar{u}(\mathbf{x})}{\partial x}. \tag{20}$$

We assume (macroscopic) cavitation, so that the fluid pressure is everywhere larger than $p_{\rm cav}$. We measure pressures relative to the atmospheric pressure and assume $p_{\rm cav} = 0$. Thus the following boundary condition must hold:

$$p_{\rm fluid} \to 0 \qquad \text{as } |\mathbf{x}| \to \infty \tag{21}$$

together with [28]

$$p_{\rm fluid} > p_{\rm cav}.$$

The elastic deformation field [25]

$$\bar{u}(\mathbf{x}) = u_0 + f(\mathbf{x}) + \frac{1}{\pi E^*}\int {\rm d}^2x'\; p_0(\mathbf{x}') \times\left(\frac{1}{|\mathbf{x}-\mathbf{x}'|} - \frac{1}{|\mathbf{x}'|}\right), \tag{22}$$

where $u_0 + f(\mathbf{x})$ is the interfacial separation for the undeformed surfaces. We take $f(\mathbf{0}) = 0$ so that u_0 is the separation in the center of the contact region.

It is convenient to introduce dimensionless quantities. Let us measure length (x and $\bar{u}$) in units of R and pressure in units of E^*. In these units, for a ball on a flat the equations above take the form

$$p_0(\mathbf{x}) = p_{\rm cont}(\mathbf{x}) + p_{\rm fluid}(\mathbf{x}), \tag{23}$$

$$p_{\rm cont}(\mathbf{x}) \approx \beta\exp\left(-\alpha\bar{u}(\mathbf{x})\frac{R}{h_{\rm rms}}\right), \tag{24}$$

$$\nabla\cdot\left(\bar{u}(\mathbf{x})^3\nabla p_{\rm fluid}(\mathbf{x})\right) = \lambda\frac{\partial\bar{u}(\mathbf{x})}{\partial x}, \tag{25}$$

$$\bar{u}(\mathbf{x}) = u_0 + f(\mathbf{x}) + \frac{1}{\pi}\int {\rm d}^2x'\; p_0(\mathbf{x}') \times\left(\frac{1}{|\mathbf{x}-\mathbf{x}'|} - \frac{1}{|\mathbf{x}'|}\right), \tag{26}$$

$$f(\mathbf{x}) = 1 - \sqrt{1-x^2-y^2},$$

$$\int_{-\infty}^{\infty} {\rm d}^2x\; p_0(\mathbf{x}) = \frac{F_{\rm N}}{R^2E^*}, \tag{27}$$

which depend on the dimensionless parameters $\lambda = 6\eta v_0/(E^*R)$, $F_{\rm N}/(E^*R^2)$ and on the parameters α and β which are determined by the surface roughness power spectrum $C(q)$.

The frictional shear stress is given by (13) with the fluid contribution

$$\boldsymbol{\sigma}_{\rm fluid}(\mathbf{x}) = \eta\left.\frac{\partial\mathbf{v}(\mathbf{x},z)}{\partial z}\right|_{\rm wall}. \tag{28}$$

The velocity profile in the gap (in the absence of wall slip):

$$\mathbf{v}(\mathbf{x}) = \frac{1}{2\eta}\nabla p_{\rm fluid}(\mathbf{x})z\,[z-\bar{u}(\mathbf{x})] + \mathbf{v}_0\frac{z}{\bar{u}(\mathbf{x})}.$$

The nominal shear stress acting on the solid walls (see footnote 3)

$$\boldsymbol{\sigma}_{\rm fluid}(\mathbf{x}) = \pm\nabla p_{\rm fluid}(\mathbf{x})\frac{\bar{u}(\mathbf{x})}{2} + \frac{\eta\mathbf{v}_0}{\bar{u}(\mathbf{x})}, \tag{29}$$

where the $+$ and $-$ signs refer to the surface $z = \bar{u}$ and $z = 0$, respectively. Because of the plane symmetry of the problem, the resultant friction force acts only along the sliding direction. The friction coefficient μ is determined by

$$\mu\, F_{\rm N} = \int {\rm d}^2x\;\sigma_{\rm f}(\mathbf{x}), \tag{30}$$

where the frictional shear stress $\sigma_{\rm f}$ was defined in section 2.

Depending on the lubricant supply, the integration of (29) should be done over the whole surface or only over the non-cavitating region. The main difference is the Couette friction contribution (the term on the RHS of (29) which explicitly depend on the sliding velocity) (see [29] for more details). In this work we assume a flooded condition in the cavitation zone, but the main results are not sensibly affected by this assumption. The equations above are conveniently solved numerically as described in appendix D.

In figures 18–22 we show the solid and fluid pressure distributions and surface separation for increasing sliding velocities, 1.31×10^{-3}, 1.18×10^{-2} and 2.00 m s^{-1}. We show two-dimensional cross sections along the sliding direction (x axis) and normal to the sliding direction (y axis), and also a three-dimensional plot (xy plane). The parameters used in the calculation are given in the figure caption of figure 18.

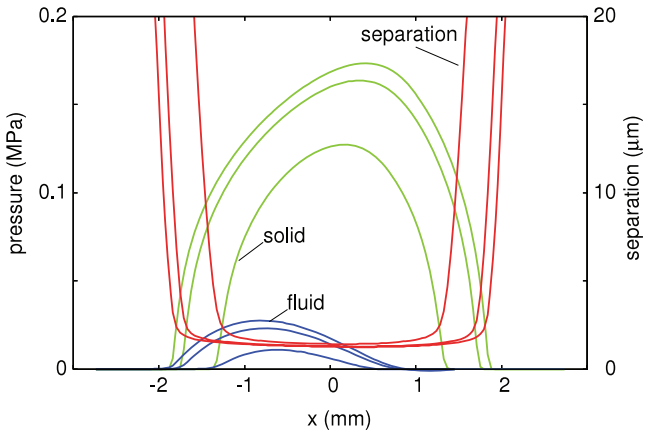

Figure 18. The contact pressure distribution and the interfacial separation between an elastic ball (reduced elastic modulus $E^* = 1.6$ MPa) and a nominal flat substrate with the root-mean-square roughness 1.6 μm at three different x–z cross sections, $y = 0$, 0.642 and 1.28 mm. The ball radius $R = 1$ cm and the loading force $F_N = 1.3$ N. The half-width of the Hertz contact area is $a_H = 1.83$ mm and the maximum and average Hertz contact pressure are 0.186 MPa and 0.124 MPa, respectively. The roughness is a self-affine fractal surface with the root-mean-square roughness 1.6 μm and with $q_0 = 2 \times 10^5$ m^{-1} and $q_1 = 0.78 \times 10^{10}$ m^{-1} and fractal dimension $D_f = 2.2$. The fluid viscosity $\eta = 0.1$ Pa s. Sliding velocity $v = 1.31 \times 10^{-3}$ m s^{-1}. The computational range is $[-1.5a_H, 1.5a_H] \times [-1.5a_H, 1.5a_H]$ with 129 × 129 grid points.

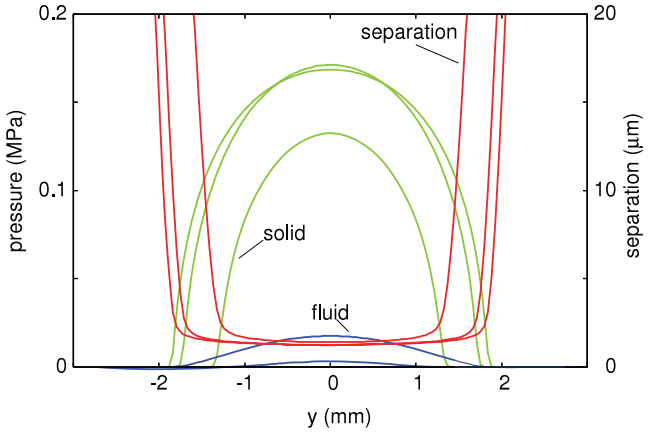

Figure 19. The same as figure 18 but with y–z cross sections, $x = 0$, 0.642 and 1.28 mm.

In figures 23, 24 we show the total contact pressure for different sliding velocities. Note that, independent of if the fluid pressure is higher or lower than the solid pressure, $p_0(x)$ (the sum of fluid pressure and asperity contact pressure) is Hertzian-like (with a small broadening at the edges because of the surface roughness and fluid leakage). This result is, of course, expected as long as the surface separation is small compared to the diameter of the Hertzian-like contact region.

Figure 25 shows the friction coefficient, μ, as a function of the product of the sliding velocity and the fluid viscosity, ηv, on a log–log scale. The calculation is for the same system as in figure 18 but for three different root-mean-square roughness values, 1, 1.6 and 3.6 μm. Note that, as expected,

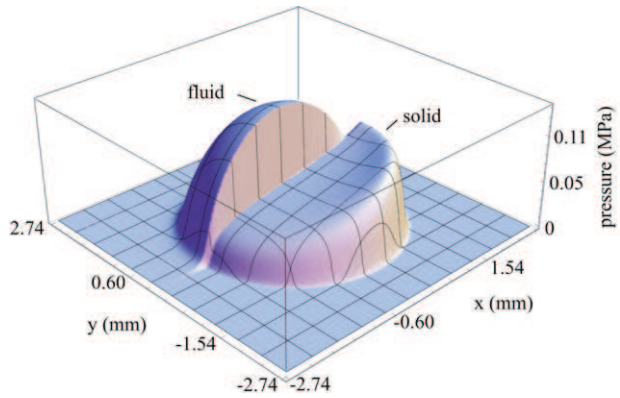

Figure 20. Fluid and asperity contact pressure surfaces for the same parameters of figure 18 but for the sliding velocity $v = 11.8 \times 10^{-3}$ m s^{-1}. Because of the contact geometric symmetry, only half the surface is shown for each field.

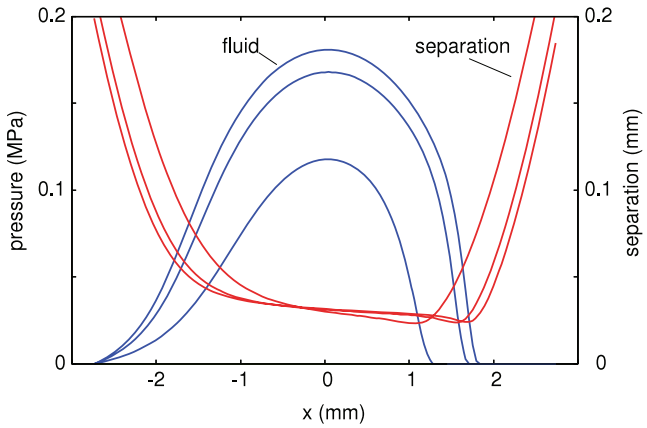

Figure 21. The same as figure 18 but for the sliding velocity $v = 2$ m s^{-1}.

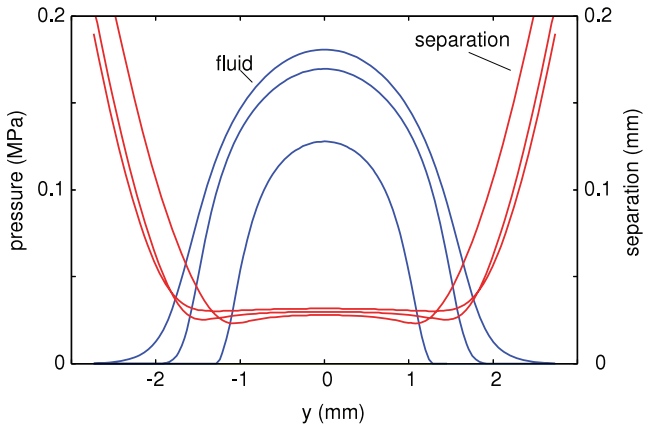

Figure 22. The same as figure 19 but for the sliding velocity $v = 2$ m s^{-1}.

when the surface roughness decreases, the minimum in the $\mu = \mu(v)$ curve is shifted to lower velocities. This is easy to understand since, in the limiting case of perfectly smooth surfaces, within continuum hydrodynamics, the surfaces will always be separated by a thin fluid film, and the minimum in

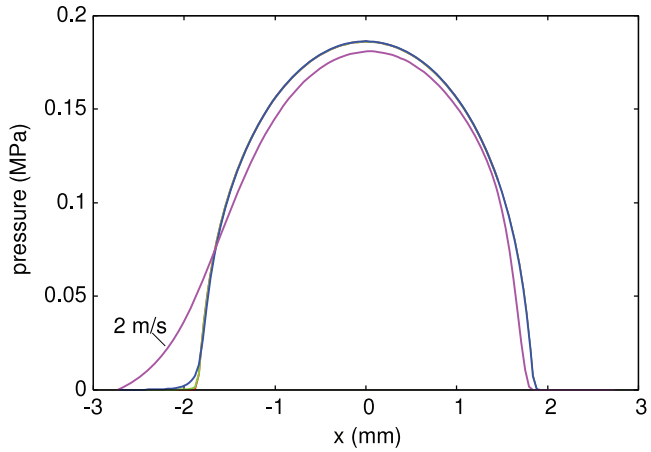

Figure 23. Total pressure, for x–z cross section at $y = 0$, for different sliding velocities (1.16×10^{-6}, 1.31×10^{-3}, 11.8×10^{-3}, 2 m s^{-1}). The red line corresponds to the highest velocity. The lower velocities overlap each other. The input parameters are the same as figure 18.

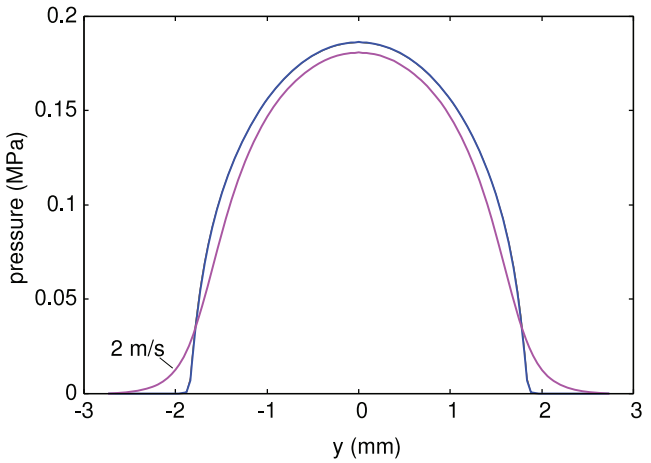

Figure 24. Total pressure, for y–z cross section at $x = 0$, for different sliding velocities (1.16×10^{-6}, 1.31×10^{-3}, 11.8×10^{-3}, 2 m s^{-1}). The red line corresponds to the highest velocity. The lower velocities overlap each other. The input parameters are the same as figure 18.

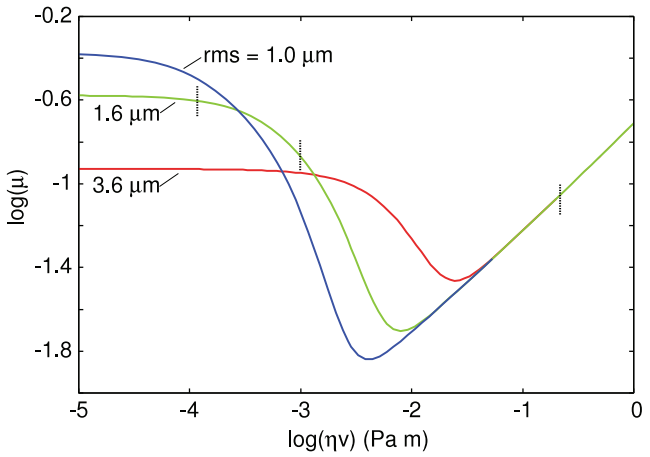

Figure 25. The friction coefficient μ as a function of the product of the sliding velocity and the fluid viscosity, ηv (log–log scale with 10 as basis). For the same system as in figure 18 but for three different root-mean-square roughness values, 1.0, 1.6 and 3.6 μm and $\sigma_1 = 1$ MPa. The vertical dashed lines correspond to the pressure and separation fields of figures 18, 20 and 21.

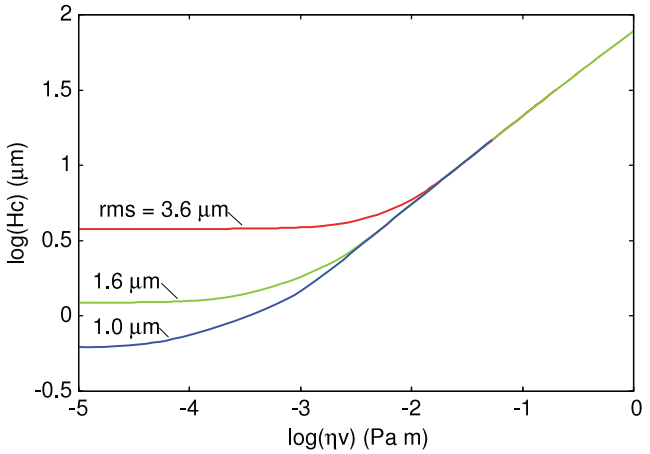

Figure 26. The central separation as a function of the product of the sliding velocity and the fluid viscosity, ηv (log–log scale with 10 as basis). For the same system as in figure 18 but for three different root-mean-square roughness values, 1.0, 1.6 and 3.6 μm.

friction (and the surface separation) is located at zero sliding velocity.

Figures 26 and 27 show, respectively, the central and the minimum separation as a function of ηv on a log–log scale. At high enough sliding velocity the surfaces are everywhere separated by a thin fluid film and the surface separation is then nearly independent of the surface roughness amplitude.

Figure 28 shows the fraction of the loading force carried by the fluid and by the asperity contact regions, and also the maximum fluid and asperity contact pressures, as a function of ηv (log–log scale), for the same system as in figure 18. The vertical dashed line indicates the velocity where the friction force is minimal. Note that the velocity where the friction is minimal is much higher than the velocity where the load carried by the fluid is equal to the load carried by the asperities. Note, however, that this result depends on the magnitude of the frictional shear stress σ_1 in the asperity contact regions.

Figure 29 shows the minimum and central separation as a function of ηv. In the boundary lubrication regime the fluid-induced deformation of the solid walls is negligible, and in this case the minimum separation coincides with the central separation. For high sliding velocities the axial symmetry is lost and the surface separation takes a 'horse-ear' shape.

4. Flat on flat

In the study above we have assumed that the solid–solid asperity contact regions are dry. This may be a good approximation for hydrophobic surfaces and at low enough sliding velocity where any thin fluid film in an asperity contact region may be removed by a dewetting transition [13–15], and the discussions in sections 2 and 3 are therefore most relevant for hydrophobic systems. Here we assume hydrophilic

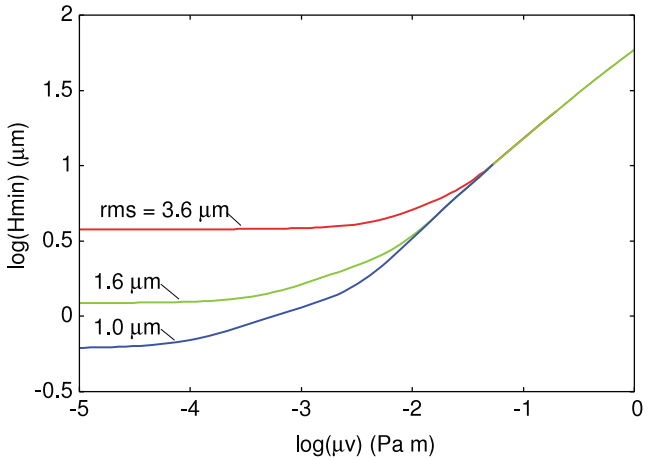

Figure 27. The minimum separation as a function of the product of the sliding velocity and the fluid viscosity, ηv (log–log scale with 10 as basis). For the same system as in figure 18 but for three different root-mean-square roughness values, 1.0, 1.6 and 3.6 μm.

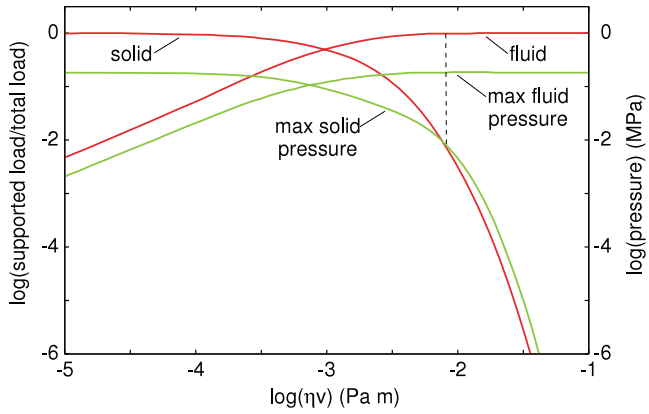

Figure 28. The supported squeezing load carried by the fluid and the asperity contact and the maximum pressure, as a function of the sliding velocity (log–log scale with 10 as basis). For the same system as in figure 18. The vertical dashed line indicates the velocity where the friction force is minimal.

surfaces. In this case the spreading pressure $S > 0$ and there will be an effective short-ranged repulsion acting between the solid walls, and unless the sliding velocity is very low and the asperity contact pressure high enough, we expect a thin fluid film in the asperity contact regions. We consider first low sliding velocities. In this case the macroscopic shape of the solid objects is of minor importance for the dependence of the sliding friction, $\mu(v)$, on the velocity v. That is, the nature of the surface separation at the inlet and at the exit of the macroscopic (or nominal) contact area has a negligible influence on $\mu(v)$ as compared to the nature of the (mainly asperity-induced) separation between the solids in the apparent contact area. In this section we will therefore assume that both solids have nominally flat surfaces [16, 17].

In the absence of cavitation and elastic deformation, fluid flow in a symmetric (around some point on the x axis) gap profile cannot support an external load, i.e. $p_{\rm fluid}(x)$ integrated over all x will vanish. However, both cavitation (if it occurs)

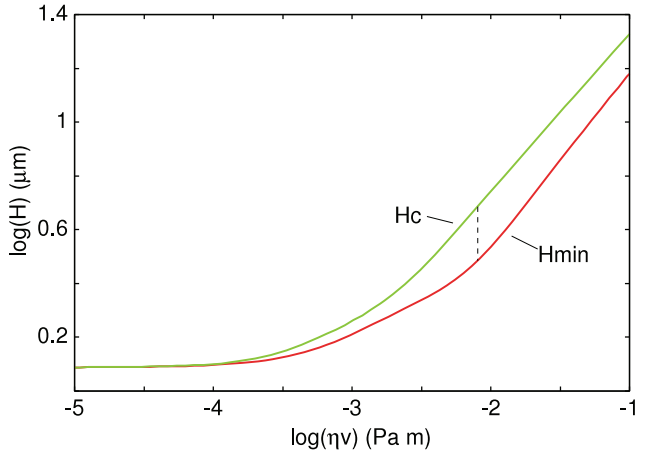

Figure 29. The minimum and central separation as a function of the sliding velocity (log–log scale with 10 as basis). For the same system as in figure 18. The vertical dashed line indicates the velocity where the friction force is minimal.

and elastic deformation of the solid walls will result in a non-zero load capacity by the fluid film (see appendix C).

Consider an elastic solid with a randomly rough surface sliding in a fluid against a flat, rigid, countersurface. Let us study the interface at the magnification ζ. Let us write the load acting on the asperities, which *appear* to be in contact with the substrate at this magnification, as $p_{\rm cont}(\zeta)A_0$. Since a part of the external load p_0A_0 is carried by the asperities and another part by the fluid in the non-contact regions we have

$$p_{\rm cont}(\zeta) = p_0 - p_{\rm fluid}(\zeta), \tag{31}$$

where $p_{\rm fluid}(\zeta)A_0$ is the load (apparently) carried by the fluid when the system is studied at the magnification ζ. Note that, when we increase the magnification, the surface area $A(\zeta)$ (the contact area observed at the magnification ζ) will decrease and the load carried by the fluid will increase. At high enough magnification the surfaces may be completely separated by a thin fluid film, and at this magnification the total load will be carried by the fluid (see figure 30). Since for infinite sized systems there are infinitely high asperities, complete non-contact will never occur in our model, but from a practical point of view this difference between the model and reality is unimportant.

An asperity contact region, which appears to be in perfect contact with the substrate at the magnification ζ, is in fact separated from the substrate with the (average) separation $u(\zeta)$ (see figure 31). In addition, during sliding the surface is slightly tilted relative to the countersurface, resulting in a local fluid pressure (see appendix C):

$$p \approx p^*_{\rm fluid} + \kappa\eta v_0 \frac{\lambda(\zeta)}{u^2(\zeta)} \tag{32}$$

where $\kappa \approx 0.2$ and where $p^*_{\rm fluid}$ is the fluid pressure at the boundary of the (apparent) asperity contact region. The resolution $\lambda(\zeta) = L/\zeta$, where L is the linear size of the system. The (apparent) load carried by the fluid when the system is studied at the magnification $\zeta + \Delta\zeta$ is given by

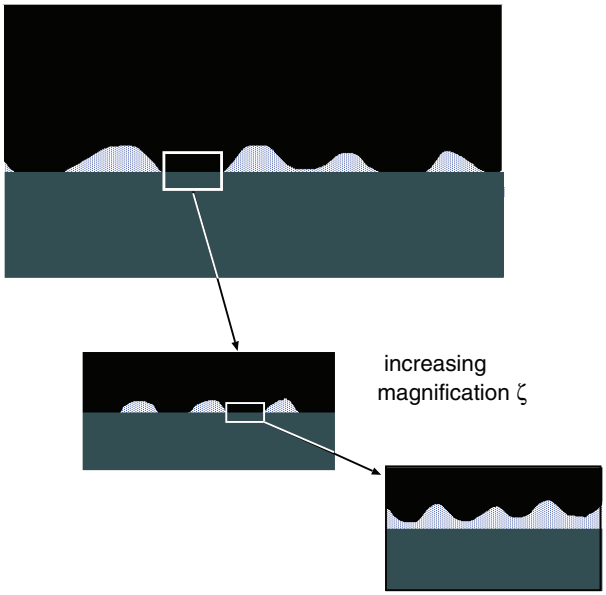

Figure 30. The asperity contact region between two solids in sliding contact in a fluid. At high enough sliding velocity, at high enough magnification the surfaces are observed to be separated by a thin fluid film.

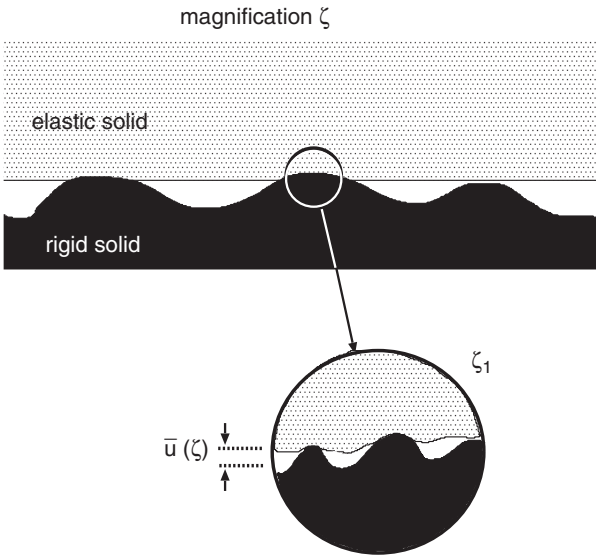

Figure 31. An asperity contact region observed at the magnification ζ. It appears that complete contact occurs in the asperity contact region, but upon increasing the magnification it is observed that the solids are separated by the average distance $\bar{u}(\zeta)$.

$p_{\rm fluid}(\zeta + \Delta\zeta)A_0$, which must be equal to the (apparent) load carried by the fluid when the system is studied at the magnification ζ, $p_{\rm fluid}(\zeta)A_0$, plus the load carried by the fluid in the surface area $A(\zeta) - A(\zeta + \Delta\zeta)$ which moves out of contact when the magnification increases from ζ to $\zeta + \Delta\zeta$. The surface separation in the newly formed non-contact surface area is $u_1(\zeta)$. Thus, using (32) it follows that

$$p_{\rm fluid}(\zeta + \Delta\zeta)A_0 \approx p_{\rm fluid}(\zeta)A_0 + [A(\zeta) - A(\zeta + \Delta\zeta)]\left[p^*_{\rm fluid}(\zeta) + \kappa\eta v_0 \frac{\lambda(\zeta)}{u_1^2(\zeta)}\right] \quad (33)$$

where $\lambda = L/\zeta$. Here the contact area, $A(\zeta)$, and the interfacial separation, $u_1(\zeta)$, at the magnification ζ, are assumed to be given by the contact mechanics theory of Persson (see below), but with the external squeezing pressure p_0 replaced with the reduced squeezing pressure $p_{\rm cont}(\zeta) = p_0 - p_{\rm fluid}(\zeta)$, which takes into account that part of the external load is carried by the fluid. In reality, the fluid pressure and the asperity contact pressure do not act uniformly at the interface so the present approach is a mean-field theory. We will take $p^*_{\rm fluid}(\zeta)$ to be the average fluid pressure observed at the magnification ζ so that $p^*_{\rm fluid}(\zeta)[A_0 - A(\zeta)] = p_{\rm fluid}(\zeta)A_0$. Substituting this in (33) gives

$$p'_{\rm fluid}(\zeta) \approx -p_{\rm fluid}(\zeta)\frac{A'(\zeta)}{A_0 - A(\zeta)} - \frac{A'(\zeta)}{A_0}\kappa\eta v_0 \frac{\lambda(\zeta)}{u_1^2(\zeta)}.$$

Integrating this equation gives

$$p_{\rm fluid}(\zeta) \approx \int_1^\zeta {\rm d}\zeta' \left[-\frac{A'(\zeta')}{A_0}\right]\frac{A_0 - A(\zeta)}{A_0 - A(\zeta')}\kappa\eta v_0 \frac{\lambda(\zeta')}{u_1^2(\zeta')}. \quad (34)$$

The effective frictional stress is given by

$$\sigma_{\rm f} \approx \frac{A(\zeta_1)}{A_0}\sigma_1 + \int_1^{\zeta_1} {\rm d}\zeta \left[-\frac{A'(\zeta)}{A_0}\right]\frac{\eta v_0}{u_1(\zeta)}. \quad (35)$$

The highest magnification ζ_1 in this equation should be chosen so that $u_1(\zeta_1)$ is of the order of nanometers, since one cannot expect fluid continuum mechanics to be valid for fluid films when the thickness becomes smaller than $\sim$1 nm, i.e. of the order of the molecular diameter of the fluid molecules. In fact, surface force apparatus measurements [31, 34] (and molecular dynamics calculations [13]) have sometimes shown deviation from bulk fluid behavior when the trapped fluid film is several nanometers thick. In principle, such effects (if known from measurements or computer simulations) can be taken into account in the formalism developed above, e.g. by using a viscosity which depends on the magnification (which can be related to the film thickness, i.e. $u = u_1(\zeta)$ can be inverted to $\zeta = \zeta_1(u)$). In the numerical simulations presented below we have chosen ζ_1 so that $u_1(\zeta_1) = 1$ nm, and assumed that the viscosity is independent of the film thickness for $u > 1$ nm.

To complete the theory we need to give the equations from which we can calculate $A(\zeta)$ and $u_1(\zeta)$. We will use contact mechanics theory developed by Persson [18, 20–23], but with the asperity load $A_0 p_{\rm cont}(\zeta)$ now depending on the magnification ζ (in the original theory there was no fluid at the interface and the load carried by the asperities was independent of the magnification). The (apparent) relative contact area $A(\zeta)/A_0$ at the magnification ζ is given by [18, 19]

$$\frac{A(\zeta)}{A_0} = \frac{1}{(\pi G)^{1/2}}\int_0^{p_{\rm cont}} {\rm d}\sigma\ {\rm e}^{-\sigma^2/4G} = {\rm erf}\left(\frac{p_{\rm cont}}{2G^{1/2}}\right)$$

where $p_{\rm cont} = p_{\rm cont}(\zeta)$ is given by (31) and where

$$G(\zeta) = \frac{\pi}{4}\left(\frac{E}{1-\nu^2}\right)^2 \int_{q_0}^{\zeta q_0} {\rm d}q q^3 C(q)$$

where the surface roughness power spectrum [30]

$$C(q) = \frac{1}{(2\pi)^2}\int {\rm d}^2x \langle h(\mathbf{x})h(\mathbf{0})\rangle {\rm e}^{-{\rm i}\mathbf{q}\cdot\mathbf{x}}$$

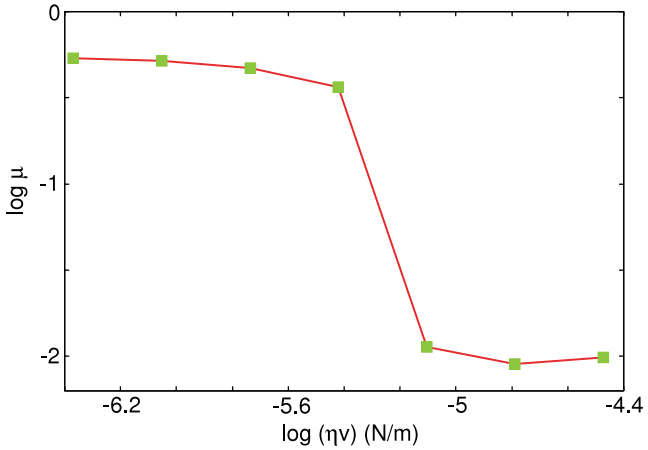

Figure 32. The friction coefficient as a function of the logarithm (with 10 as basis) of the product between the fluid viscosity η and the sliding velocity v. For an elastic solid (elastic modulus $E = 10$ MPa) with a flat surface in contact with a hard substrate with a self-affine fractal surface with the fractal dimension $D_f = 2.2$ and the root-mean-square (rms) roughness 1 μm. The fluid viscosity $\eta = 0.1$ Pa s.

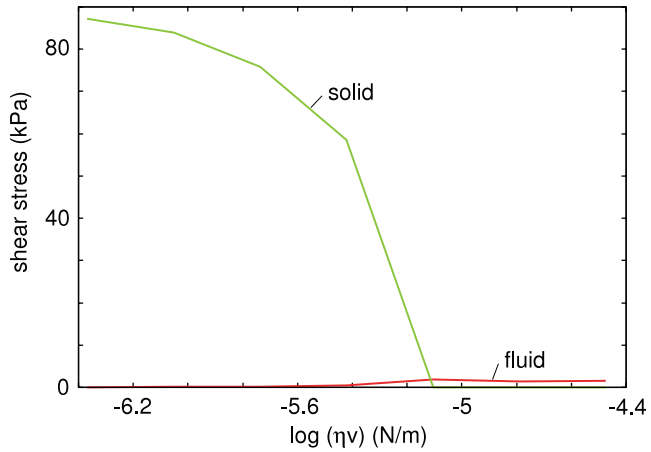

Figure 33. The (nominal) frictional shear stress from the solid contact area and from the fluid as a function of the logarithm (with 10 as basis) of the product between the fluid viscosity η and the sliding velocity v. For the same system as in figure 32.

where $\langle \cdots \rangle$ stands for ensemble average. Here E and ν are the Young's elastic modulus and the Poisson ratio of the rubber. The height profile $h(\mathbf{x})$ of the rough surface can be measured routinely today on all relevant length scales using optical and stylus experiments.

We define $u_1(\zeta)$ to be the (average) height separating the surfaces which appear to come into contact when the magnification decreases from ζ to $\zeta - \Delta\zeta$, where $\Delta\zeta$ is a small (infinitesimal) change in the magnification. $u_1(\zeta)$ is a monotonically decreasing function of ζ, and can be calculated from the average interfacial separation $\bar{u}(\zeta)$ and $A(\zeta)$ using (see [23])

$$u_1(\zeta) = \bar{u}(\zeta) + \bar{u}'(\zeta)A(\zeta)/A'(\zeta).$$

The quantity $\bar{u}(\zeta)$ is the average separation between the surfaces in the apparent contact regions observed at the magnification ζ, see figure 31. It can be calculated from [23]

$$\bar{u}(\zeta) = \sqrt{\pi}\int_{\zeta q_0}^{q_1} \mathrm{d}q\, q^2 C(q) w(q) \times \int_{p(\zeta')}^{\infty} \mathrm{d}p' \frac{1}{p'}\left[\gamma + 3(1-\gamma)P^2(q, p', \zeta)\right] \mathrm{e}^{-[w(q,\zeta)p'/E^*]^2},$$

where $\zeta' = q/q_0$ and where γ is of order unity (but never larger than unity; we use $\gamma \approx 0.4$) and where

$$p(\zeta) = p_{\mathrm{cont}}(\zeta)A_0/A(\zeta)$$

and

$$w(q, \zeta) = \left(\pi \int_{\zeta q_0}^{q} \mathrm{d}q'\, q'^3 C(q')\right)^{-1/2}.$$

The function $P(q, p, \zeta)$ is given by

$$P(q, p, \zeta) = \frac{2}{\sqrt{\pi}} \int_0^{s(q,\zeta)p} \mathrm{d}x\, \mathrm{e}^{-x^2},$$

where $s(q, \zeta) = w(q, \zeta)/E^*$.

When we study the apparent contact area at increasing magnification, the contact pressure $p(\zeta)$ will increase and the average separation $\bar{u}(\zeta)$, between the surfaces in the (apparent) contact regions observed at the magnification ζ will decrease.

In figure 32 we show the friction coefficient μ as a function of the logarithm (with 10 as basis) of the product ηv between the fluid viscosity η and the sliding velocity v. The result is for an elastic solid (elastic modulus $E = 10$ MPa) with a flat surface in contact with a hard substrate with the root-mean-square (rms) roughness 1 μm. We have assumed that the frictional shear stress in the area of real contact is $\sigma_1 = 1$ MPa. The area of real contact is now defined as the surface area where the separation $d < 1$ nm. Since for hydrophilic surfaces most likely a monolayer, or two, of the liquid molecules are adsorbed on the solid walls, there is, of course, no reason for σ_1 to be the same as for hydrophobic surfaces. Note the abrupt drop in the friction at $v \approx 50$ μm s^{-1}. We will denote this effect as viscous hydroplaning.

In figure 33 we show the (nominal) frictional shear stresses $\sigma_{\mathrm{cont}}(\zeta_1)$ and $\sigma_{\mathrm{fluid}}(\zeta_1)$, resulting from the solid contact area and from the fluid regions, respectively, as a function of the logarithm (with 10 as basis) of ηv. Note the abrupt drop in the solid frictional shear stress at the onset of viscous hydroplaning.

In figures 34 and 35 we show the (nominal) contact pressure, p_{cont}, and the (normalized) area of contact, A/A_0, respectively, as a function of the logarithm (with 10 as basis) of the magnification. The curves are for the velocities (from top to bottom) 4.3, 8.9, 18.3, 37.9, 78.5, 162 and 336 μm s^{-1}. Note that, when the velocity is above the threshold of viscous hydroplaning (i.e. $v > 50$ μm s^{-1}), at the highest magnification the nominal contact pressure, and the area of solid contact both vanish, i.e. all the asperity 'contact' regions are separated by more than 1 nm, and (thin) fluid films exist in all the asperity contact regions, resulting in the small friction observed for $v > 50$ μm s^{-1}.

The discussion presented in this section is a first attempt to address a very complex problem using a new novel approach.

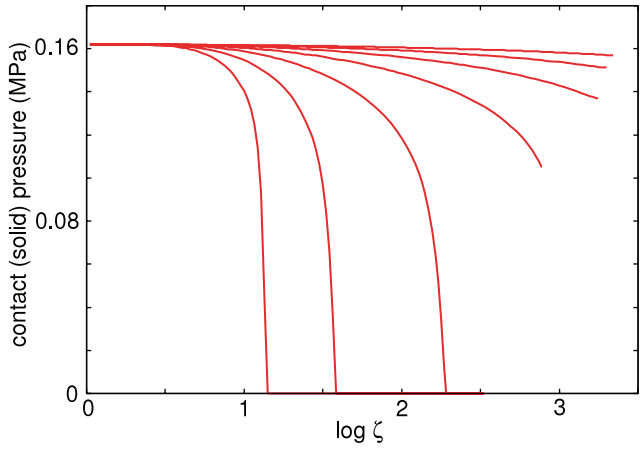

Figure 34. The (nominal) contact (solid) pressure as a function of the logarithm (with 10 as basis) of the magnification. For the same system as in figure 32. The curves are for the velocities (from top to bottom) 4.3, 8.9, 18.3, 37.9, 78.5, 162 and 336 μm s^{-1}.

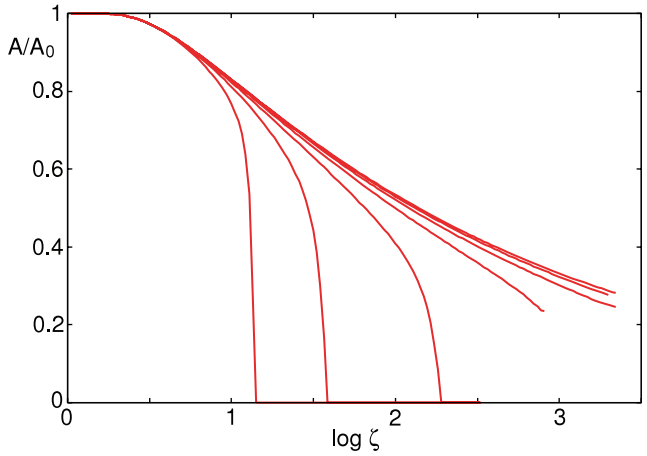

Figure 35. The normalized (apparent) contact area A/A_0 as a function of the logarithm (with 10 as basis) of the magnification. For the same system as in figure 32. The curves are for the velocities (from top to bottom) 4.3, 8.9, 18.3, 37.9, 78.5, 162 and 336 μm s^{-1}.

The theory can be improved and extended in various ways:

(a) The effective shear viscosity of thin confined fluid films often depends on the thickness of the film, at least when the film thickness becomes of the order of nanometers [13]. Thus, fluid molecules confined between smooth parallel surfaces are known to form layers parallel to the surfaces [13, 31]. It is possible, if necessary, to use a fluid viscosity η which depends on the local fluid film thickness $u = u(\mathbf{x})$, i.e. $\eta = \eta(u)$ [2]. Since the surface separation $u = u_1(\zeta)$ depends on the magnification ζ we can consider $\eta = \eta(\zeta)$ as a function of ζ and using this in all the expressions above will account for the dependence of the viscosity on the film thickness. It is also easy to include a dependence of η on the local pressure or shear rate, if necessary.

(b) In the study above we have assumed nominally flat surfaces. However, if the (important) roughness occur on length scales much smaller than the radius of curvatures of the nominal surfaces of the (macroscopic) solids under consideration (e.g. the radius of curvature of a ball in a ball bearing), then the theory developed below can be applied to this situation too by solving, together with equation (34), an (average) mass conservation equation (a Reynolds-like equation with flow factor corrections), but this will be shown elsewhere. In this case the contact pressure and the fluid pressure will depend not only on the magnification but also on the spatial coordinate $\mathbf{x}$ in the nominal contact area, i.e. $p_{\rm cont} = p_{\rm cont}(\zeta, \mathbf{x})$ and $p_{\rm fluid} = p_{\rm fluid}(\zeta, \mathbf{x})$ with

$$p_{\rm cont}(\zeta, \mathbf{x}) + p_{\rm fluid}(\zeta, \mathbf{x}) = p_0(\mathbf{x}).$$

The macroscopic (or nominal) contact pressure and fluid pressure are given by $p_{\rm cont}(\mathbf{x}) = p_{\rm cont}(\zeta_1, \mathbf{x})$ and $p_{\rm fluid}(\mathbf{x}) = p_{\rm fluid}(\zeta_1, \mathbf{x})$, respectively.

5. Discussion

The theory presented in sections 2 and 3 (and 4) is of the mean-field type, where the strongly fluctuating asperity contact pressure is replaced by a slowly varying (locally averaged) contact pressure $p_{\rm cont}(x)$. In addition, it is assumed that $p_{\rm cont}(x)$ is related to the local (average) separation $\bar{u}(x)$ as obtained for stationary solids without adhesion. When the spreading pressure $S < 0$ an effective adhesion occurs between the solids. This effect can be taken into account by using the relations between $\bar{u}$ and the squeezing pressure p_0, and between the contact area A and p_0, obtained using the formalism developed in [21], which includes adhesion (which depends on the interfacial binding energy $\gamma = -S$). However, if S is close to zero, then the adhesional effect will be small. Thus, the results presented in sections 2 and 3 should hold as long as the magnitude of S is small enough (but S negative).

In figure 36 we compare the Couette friction coefficient as measured by Bongaerts *et al* [32] (for a PDMS rubber ball sliding on a PDMS disc), with the prediction of the model of section 3, with a dry shear stress $\sigma_1 = 1$ MPa. In our calculation we assume a physically reasonable roughness power spectral density $C(q)$, with the same rms roughness amplitude as the measured one. The theory of section 3 does not include the fluid-induced deformation of asperities (see section 4), but the agreement between theory and experiment in the boundary and mixed region is nevertheless relatively good. The reason for this may be that the asperity contact regions tend to be dry due to dewetting transitions, as expected for hydrophobic systems at low sliding velocities.

In the hydrodynamic range the slope of the calculated relation between v and μ agree perfectly with the measured slope, but the magnitude differs by about a factor $\sim$2. The reason of the latter difference may, at least in part, be related to the different adopted geometrical set-up in the experiment [32] as compared to our model. Indeed in our model the ball and substrate velocities are always constant (say, ball sliding in the x direction on the flat countersurface), while in the experiment the ball is rotating (with slip) following a circular track on the substrate, and this difference can be important when, say, the ball radius is comparable to the disc radius. Moreover, some starvation may also affect the set-up and reduce the mean oil

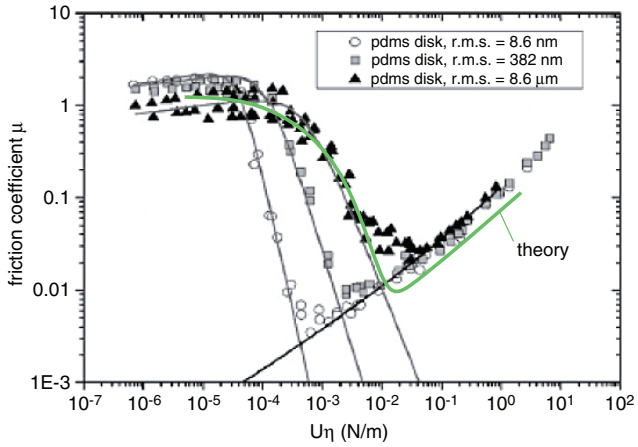

Figure 36. Friction coefficient for PDMS–PDMS interaction from [32]. The green curve (theory) corresponds to the predicted Couette friction from the theory of section 3. Adopted parameter: reduced elastic modulus $1/E^* = (1-\nu_a^2)/E_a + (1-\nu_b^2)/E_b$, $E^* = 1.6$ MPa, radius $R = 0.95$ cm, loading force $F_N = 1.3$ N, sliding-to-roll-ratio 0.5. The roughness is a self-affine fractal surface with the root-mean-square roughness 3.6 μm and with $q_0 = 1 \times 10^4$ m^{-1} and $q_1 = 0.78 \times 10^{10}$ m^{-1} and fractal dimension $D_f = 2.2$. The computational range is $[-4.25a_H, 1.5a_H] \times [-3a_H, 3a_H]$ with 116×121 grid points.

gap between surfaces; this will directly increase the measured Couette friction.

In the study above we have assumed that a frictional shear stress σ_1 acts in the area of real (or atomic) contact. This is a reasonable assumption if the hard solid (substrate) is flat and smooth (no surface roughness), while the rubber surface has surface roughness. In this case the same rubber asperities will be in contact with the substrate at all times and no (asperity-induced) time-dependent deformation of the rubber will occur. Thus, as the surface roughness amplitude increases the area of real contact will decrease and the contribution to the friction from the asperity contact region will decrease. On the other hand, when the (hard) substrate is rough, the friction may increase as the surface roughness increases. This results from the fact that, as the rubber slides in contact with a hard substrate asperity, the asperity will generate time-dependent deformations of the rubber which, because of the internal friction in the rubber, will contribute to the sliding friction [18, 33]. If the rubber is very lossy for the relevant perturbing frequencies, the asperity contribution may dominate the friction for low sliding velocity (boundary lubrication), in which case the sliding friction will increase with increasing surface roughness, even if the area of real (atomic) contact decreases. The same behavior is also expected even if a fluid film separates the surfaces, assuming that the film thickness is much smaller than the substrate roughness amplitude (see section 6). We note that, while in static contact, the original system can be replaced by an elastic solid with a smooth surface in contact with a rigid solid with a rough surface given by the combined surface roughness of the original system: this is in general not true for surfaces in relative motion.

For hydrophobic systems, the theory presented in sections 2 and 3 cannot be applied for perfectly smooth surfaces. For this limiting case there is likely to be hysteresis in the $\mu(v)$ curve between the case where the velocity increases from a very small value (corresponding to dry contact) and the case when the velocity decreases from a high velocity (corresponding to lubricated contact). The first case has been studied by Martin *et al* [27]. It was found that the transition from dry contact to lubricated contact occurs in a narrow velocity range (less than a factor of 2 change in the velocity). This is in sharp contrast to the case studied in section 2 where, even for the smoothest surface, the transition occurs gradually over nearly two decades in velocity. Martin *et al* found that the transition velocity is determined approximately by the condition that the velocity of 'forced wetting' (given by the sliding velocity v) equals the dewetting velocity v_{dewet} observed for the case of stationary surfaces (i.e. $v = 0$). This assumption results in a transition from dry contact to lubricated contact as the sliding velocity increases in a narrow velocity region around [27]

$$v_c \approx \left(\frac{|S|^4}{\eta^3 E R}\right)^{1/3}.$$

When the sliding velocity is lowered, the transition to dry contact is likely to occur at a lower sliding velocity than v_c and will be induced by thermally activated fluctuations, which may result in the nucleation of the fluid 'squeeze-out'. In this case the transition to dry contact should also depend on the speed with which the velocity is reduced.

In the theory presented in sections 2 and 3 it is assumed that the area of real contact is dry, i.e. it is assumed that the sliding velocity in the mixed lubrication region is below the dewetting velocity in the asperity contact regions. For hydrophilic surfaces the situation is more complex and the surfaces are probably nearly never perfectly dry, but at least one or two monolayers of 'fluid' may cover the sliding surfaces even in the 'area of real contact' [13]. This will modify (as compared to perfectly dry surfaces) the frictional shear stress in the area of real contact. In addition, for very thin fluid films (which may never occur for hydrophobic surfaces due to dewetting already at a finite fluid film thickness), the viscosity of the fluid may be modified due to layering of the molecules parallel to the hard substrate, see [2]. Such layering is known to modify the effective shear viscosity of the fluid [34] and may also result in 'quantized' squeeze-out of the 'fluid' where individual monolayers of fluid molecules are squeezed out from the interface in abrupt transitions at rather well-defined critical normal pressures [13, 34]. Clearly, such effects can be taken into account in the theory of mixed lubrication for hydrophilic surfaces (section 3) only when these 'last-monolayers' properties, which result from the fluid–solid wall interaction, are known from experiments [13, 34] or computer simulations (e.g. molecular dynamics) [13].

6. Applications

Here we will briefly consider two applications of the theory presented above, namely to sliding friction for (a) rubber wiper blades, and (b) tires on lubricated road surfaces.

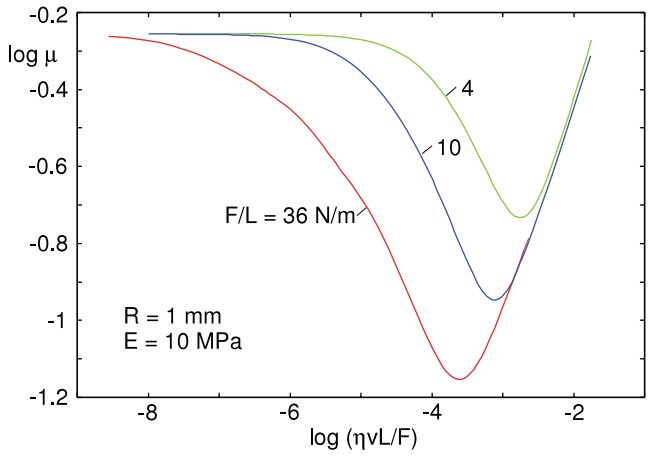

Figure 37. Friction coefficient as a function of $\eta v L/F$ (on a log scale with 10 as basis) for rubber sliding on a hard substrate for three different loads (per unit length): $F/L = 4$, 10 and 36 N m^{-1}. The rubber cylinder has the radius $R = 0.001$ m and the same surface roughness as in figure 4. The fluid viscosity $\eta = 0.001$ Pa s. With increasing load, the Hertzian average pressure and the half-width of the Hertz contact area increases from 0.10 MPa, 20 μm (for $F/L = 4$ N m^{-1}), 0.16 MPa, 31 μm (for $F/L = 10$ N m^{-1}) to 0.31 MPa and 59 μm (for $F/L = 36$ N m^{-1}).

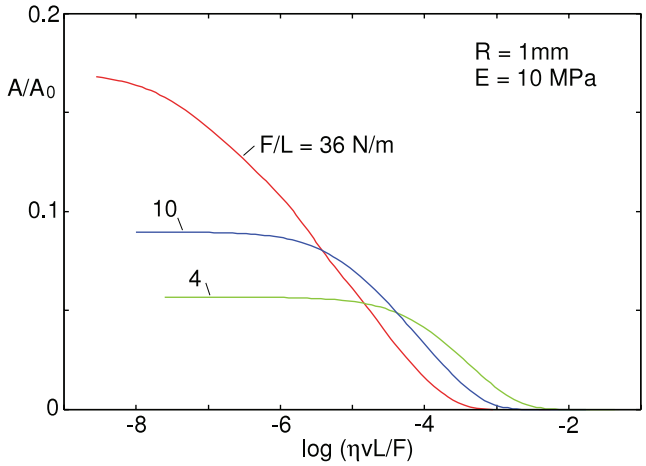

Figure 38. The relative (projected) contact area as a function of the logarithm of $\eta v L/F$. For the same system as in figure 37.

Wiper blades

Rubber wiper blades are used to remove water from glass windows. After some use the rubber blades typically develop (because of wear) a surface roughness with an rms amplitude of the order of one micrometer. Consider a rubber cylinder with radius $R = 1$ mm sliding on a rigid flat substrate. We assume the rubber cylinder to have the same surface roughness as for the system studied in figure 4 (i.e. the rms roughness is 1 μm and the Hurst exponent $H = 0.8$). In figure 37 we show the dependence of the friction coefficient μ on the parameter $\eta v L/F$ for three different loads (per unit length): $F/L = 4$, 10 and 36 N m^{-1}. At high velocity (in the hydrodynamic region) the three cases give (almost) the same behavior, but they differ drastically in the mixed lubrication region. For very low sliding velocities (the boundary lubrication region) the three cases give

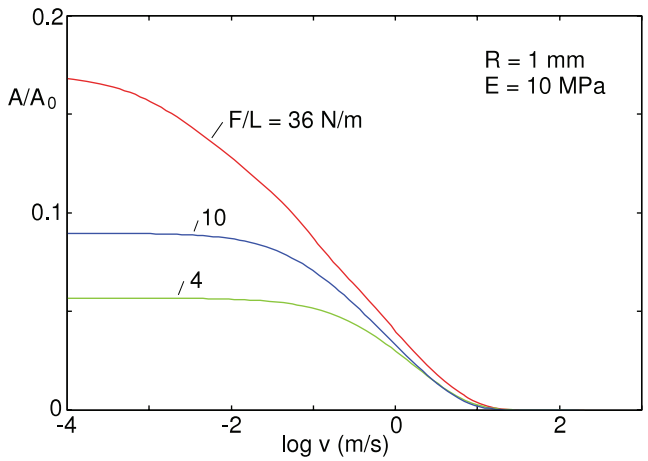

Figure 39. The relative (projected) contact area as a function of the logarithm of the sliding velocity. For the same system as in figure 37.

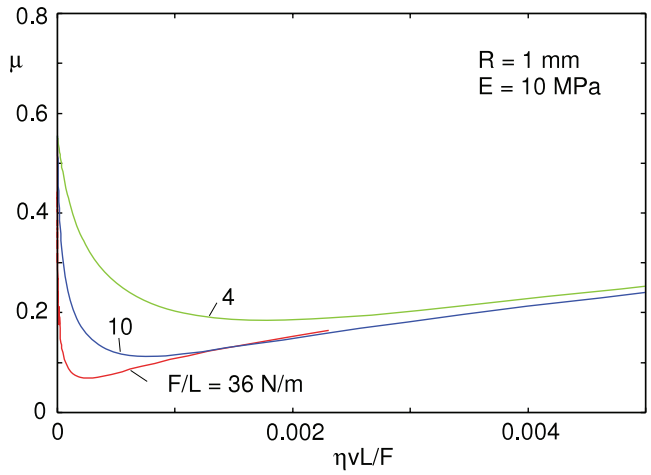

Figure 40. The same as in figure 37 but with a linear scale.

again similar results, but this holds in the present case only because the area of real contact is proportional to the load. For smoother surfaces (or for higher loads) this is no longer the case as the area of real contact will depend nonlinearly on the load.

Figures 38 and 39 show, for the same system as in figure 37, the relative (projected) contact area as a function of the logarithm of $\eta v L/F$ and as a function of v, respectively. Note that the relative contact area for low sliding velocities depends nonlinearly on the load, but this is due to the increase of the nominal contact area A_0 with increasing load ($A_0 \sim F^{1/2}$ for cylinder contact), and A is in fact proportional to the load in the present case (see above).

In figure 40 we show the same as in figure 37 but on a linear scale. The results presented in this figure are very similar to the results obtained by Koenen *et al* [35, 36] for rubber wiper blades (see figure 41), although in this application it is likely that the surfaces are smoother and the rubber elastic modulus is higher than used in our model calculation. In addition, the radius of curvature of the rubber edge in contact with the glass surface is likely to be smaller than $R = 1$ mm used above.

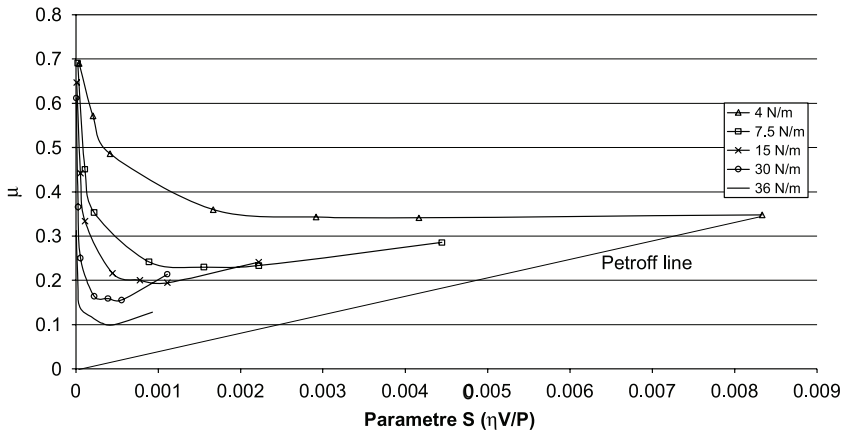

Figure 41. Friction coefficient as a function of the Sommerfeld parameter $\eta v/P$. Reproduced from [35]. Copyright 2007 with permission from Elsevier.

Tires

The friction between a tire and a road surface is mainly due to the time-dependent deformation of the rubber by the road surface asperities. That is, during slip the road asperities will generate time-dependent (pulsating) forces acting on the rubber surface and, because of the internal friction in the rubber, some part of the deformation energy will be transformed into heat. Since road surfaces have surface roughnesses over a large range of length scales (say, from cm to nm), the tire–road friction will have contributions from rubber deformations over a wide distribution of length scales.

When the contact between a tire and a road is observed at increasing magnification, the area of real contact will monotonically decrease. At some high magnification, typically corresponding to a resolution (or wavelength λ_c) of the order of micrometers, the stresses and the temperature increase during slip will be so high that bonds in the rubber will rupture resulting in, for example, micrometer sized cracks and wear processes. In the theory of rubber friction we have developed, we only take into account the asperity-induced deformation of the rubber down to the length scale λ_c. The range of surface roughness length scales (or wavelength) which contributes to the friction will change from one surface to another in such a way that at the resolution λ_c the stresses (and the temperature increase) at the rubber surface corresponds to the rupture limit. This theory explains why the tire–road friction varies very little between different (clean and dry) road surfaces [37, 38], in spite of large changes in the surface topography and root-mean-square roughness. Thus, a smoother road surface will (in comparison to a surface with larger roughness), in general, result in a smaller cutoff λ_c, and a larger range of surface roughness wavelength components will contribute to the friction in such a way that there is only a small change in the friction in most cases. On the other hand, the predicted wear rate [39], which depends on λ_c, may change tremendously between different surfaces (it tend to decrease with decreasing surface roughness amplitude, assuming no change in the 'sharpness' of the roughness), which is in good agreement with experimental observations [38].

The results above are for clean surfaces. If the tire surface is contaminated by small particles, then the cutoff length λ_c may instead be determined by the (typical) particle diameter D. Similarly, if there is a liquid on the road surface the cutoff may be determined by the liquid squeeze-out process. In this case the cutoff will depend on the thickness of the fluid layer, on the viscosity of the fluid and on the tire rolling and slip velocities. Thus, in this case the effective cutoff length λ_c is not determined by the rupture strength of the rubber and one now expects (and observes) a much larger spread in tire–road friction values between different road surfaces, and also smaller tire tread wear.

For flooded road surfaces and high enough car velocity (typically above 60 km h^{-1}) there may not be enough time to squeeze out the water between the tire and the road, resulting in a thick water film between the tire and the road and a very low friction (hydroplaning). For thick water films the squeeze-out is determined by the inertia of the water and does not depend on the water viscosity. Here we are instead interested in the much more common case where most of the water is squeezed out from the tire–road contact regions and where the squeeze-out dynamics depends on the water viscosity. In section 4 we have shown that in this case viscous hydroplaning may occur if the slip velocity is high enough. As long as the water film, which occurs in the asperity contact regions observed at the magnification ζ, is much thinner than the height of the asperities, which typically are of order[4] $h_{\rm rms}(\zeta)$, the water film has a negligible influence on the asperity-induced contribution to the rubber friction. However, when the water film thickness is of the order of the height of the asperities it will effectively smooth the road surface so that asperities, which can be observed at higher magnification, will not induce deformations of the rubber surface and will hence not contribute to the rubber friction. Thus, we conclude that the fluid film will introduce an effective cutoff so that only road surface roughness with wavelength $\lambda > \lambda_c = \lambda_0/\zeta_c$ (where λ_0 is the surface roughness power spectrum roll-off wavelength) will contribute to the

[4] The root-mean-square roughness $h_{\rm rms}(\zeta)$, due to the surface roughness components with wavevectors $q > q_0\zeta$, can be calculated from the surface roughness power spectrum using $h^2_{\rm rms} = 2\pi \int_{q_0\zeta}^{q_1} {\rm d}q\, qC(q)$.

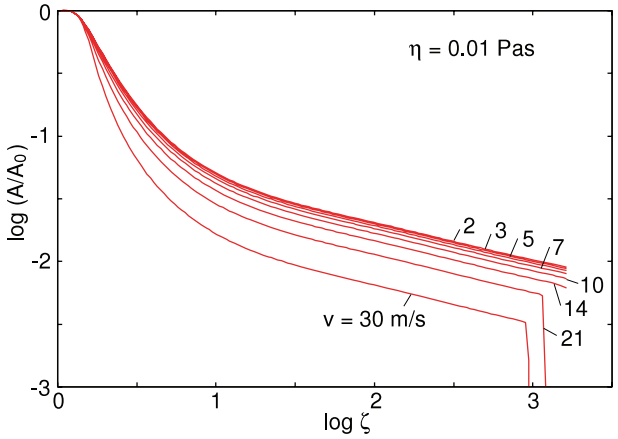

Figure 42. The logarithm (with 10 as basis) of the (normalized) contact area as a function of the logarithm (with 10 as basis) of the magnification $\zeta = q/q_0$ for a rubber block (elastic modulus $E = 10$ MPa, Poisson ratio $\nu = 0.5$) sliding on a asphalt road surface in a fluid with the viscosity $\eta = 0.01$ Pa s. Results are shown for several sliding velocities: $v = 2, 3, 5, 7, 10, 14, 21$ and 30 m s^{-1}. Note the reduction in the contact area due to viscous hydroplaning.

rubber friction, where cutoff magnification ζ_c is defined by the condition that the contact area $A(\zeta) \to 0$ as $\zeta \to \zeta_c$. In addition, the area of real contact for $\zeta < \zeta_c$ will be reduced due to the fact that part of the load will be carried by the fluid. This is illustrated in figure 42 which shows the (normalized) contact area as a function of the magnification $\zeta = q/q_0$ (log–log scale), calculated using the theory of section 4 for a rubber block (elastic modulus $E = 10$ MPa, Poisson ratio $\nu = 0.5$) sliding on an asphalt road surface in a fluid with the viscosity $\eta = 0.01$ Pa s. This fluid viscosity is higher than for clean water but may be typical of contaminated water on wet road surfaces immediately after raining has started. In the calculation we have used the measured road surface power spectrum $C(q)$ and results are shown for several sliding velocities $v = 2, 3, 5, 7, 10, 14, 21$ and 30 m s^{-1}. Note the reduction in the contact area (due to viscous hydroplaning), which is particularly strong for the two highest slip velocities. For the present road surface (new asphalt road), for clean water (viscosity $\eta \approx 0.001$ Pa s) and slip velocities $v < 30$ m s^{-1}, the viscous hydroplaning is negligible. However, even in this case there may be a reduction in the friction from water trapped (or sealed off) in cavities as discussed in [40].

There will also be a contribution to the friction from shearing the thin fluid film in the non-contact tire–road footprint, but this contribution is probably negligible in most cases. We will present detailed calculations of viscous hydroplaning for tires elsewhere.

7. Summary and conclusion

We have presented a simple description of the transition from boundary lubrication at low sliding velocities to hydrodynamic lubrication at high sliding velocities. Our treatment is based on a recently developed contact mechanics theory which takes into account the long-range elastic deformation of the solids. We first considered the sliding of elastic cylinders and spheres on nominally flat substrates. In these treatments the asperity contact regions were assumed to be dry, as expected for hydrophobic systems at low enough sliding velocities. The asperity interactions were taken to depend on the interfacial separation $\bar{u}(\mathbf{x})$ as $p_{\rm cont}(\mathbf{x}) \sim \exp(-\alpha\bar{u}(\mathbf{x})/h_{\rm rms})$ (the Greenwood–Williamson [41] contact mechanics theory predicts a relation which is Gaussian-like rather than exponential). We note that this form of the solid–solid interaction has been found to be in excellent agreement with experiment [42]. One interesting result of the analysis in section 2 is that, for elastically soft solids (such as rubber), the exact boundary condition used when solving the fluid flow problem has only a very small influence on the calculated friction. That is, whether cavitation occur or not has only a small influence on the friction; even without cavitation the fluid pressure will deform the elastic solids in such a way that the load capacity of the sliding junction is nearly independent of whether cavitation occurs or not. For elastically hard solids this is, of course, not the case and in the limit of rigid solids the load capacity (in the absence of cavitation) for a sliding junction, which is symmetric around some point along the sliding direction, will vanish.

We have also studied the case where the asperity contact regions tend to be separated by thin fluid films, as always expected for hydrophilic systems unless the sliding velocity is extremely small. For this case we assumed nominally flat surfaces, but the analysis can be easily extended to solid objects with (nominally) curved surfaces.

We have presented applications to wiper blades and also briefly discussed tire friction on wet road surfaces. The theoretical results are in good qualitative agreement with experimental data for wiper blades, while detailed calculations for tires on wet road surfaces will be presented elsewhere. The results presented above may also be applied to many other systems of interest, e.g. to rubber seals [43] and gel systems [44, 45].

Finally, we note that an accurate description of the transition from boundary lubrication to hydrodynamic lubrication for rough surfaces is a very complex problem, but we believe that the present treatment captures much of the important physics, and that it can be improved and extended in various ways.

Appendix A

If a fluid is in statistical equilibrium with the normal atmosphere, molecules from the atmosphere (mainly O_2 and N_2) are dissolved in the fluid. Thus, if in any region in the fluid the pressure would fall below atmospheric pressure, the fluid will be unstable against cavity formation. That is, a cavity would form containing gas at atmospheric pressure. The gas molecules in the cavity result from the diffusion of the atmospheric gas dissolved in the fluid into the cavity. However, cavitation in a homogeneous liquid is usually a thermally activated process. The energetic barrier to be overcome is due to the surface energy of the (small) critical 'hole' formed in the liquid. In order to nucleate a cavity in a short time, a large negative pressure (tensile stress) may be necessary.

The energy to form a small spherical hole in a liquid at the negative pressure p is $U(R) = -|p|4\pi R^3/3 + \gamma 4\pi R^2$. The maximum of $U(R)$ occurs for $R = R_c = 2\gamma/|p|$ and the barrier height $\Delta E = U(R_c) = 4\pi\gamma R_c^2/3$. The probability rate of cavitation

$$w \approx (V/a^3)\nu e^{-\Delta E/k_B T} \tag{A.1}$$

where V/a^3 is the number of 'places' where a cavity can form (V is the fluid volume, a of the order of an interatomic distance in the fluid) and ν is a frequency of order $\nu \approx 10^{12}$ s^{-1}. In order for cavitation to occur in, say, a volume $V = 1$ cm^3 and on a timescale of seconds, ΔE should be of the order of electron volts, which gives R_c of the order of a few nanometers and the pressure $p \approx -10$ MPa. Thus, unless the magnitude of the (negative) pressure is very large, it may take a long time to nucleate the cavity. However, in most practical situations the nucleation of a cavity is not a homogeneous process as assumed above, but occurs at some defect on the solid walls, or may involve some trapped air bubbles at the interface resulting, for example, from incomplete wetting. In the present case the pressure fluctuations induced by the shortest wavelength roughness are highest, so it may be that the cavities are induced first at the most narrow constrictions at the interface (but involving length scales larger than R_c). In section 3 we showed that the pressure induced in the liquid at the length scale λ is of order $p \approx \kappa\eta v_0\lambda/u^2$. Assuming $u \approx 1$ nm, $\lambda/u \approx 100$ and using $\eta = 0.1$ N s m^{-2} gives the pressure fluctuation of order 10 MPa already for the sliding velocity v_0 of order 10^{-3} m s^{-1}.

It would be very interesting to study (using optical methods) the (time-dependent) formation of cavities at the interface between a (transparent) perfectly flat glass surface sliding in a liquid in contact with a stationary rubber surface with surface roughness. We note, as a curiosity, that very large negative pressures (up to -100 MPa for high surface tension liquids such as water), may occur in (very short, $\sim$1 nm) capillary bridges. It has often been stated in the literature that this should result in cavity formation and the break-down of the capillary bridges. However, this conclusion is incorrect, since a capillary bridge is a thermodynamically stable (minimum free energy) state. Of course, strong density fluctuations (which may be interpreted as the rapid formation and collapse of small cavities) may occur in the fluid, but the capillary bridge is nevertheless stable.

Appendix B

Equations (2)–(4), (6) and (7) in section 2 are conveniently solved numerically as follows. For zero sliding velocity if $h_{rms} \ll R$ we expect the contact pressure to be Hertz-like so that

$$p_{cont} \approx p_H = \frac{2F_N}{\pi La}\left[1 - \left(\frac{x}{a}\right)^2\right]^{1/2},$$

and we get from (4)

$$\bar{u} = \frac{h_{rms}}{\alpha}\ln\left(\frac{\beta E^*}{p_H}\right),$$

which is our starting value for $\bar{u}(x)$. Next we increase the sliding velocity v_0 in (very small) steps Δv as follows:

First put $v_0 = 0$ and put u^* large enough.

Start

Replace $v_0 \to v_0 + \Delta v$. Calculate the fluid pressure

$$p_{fluid}(x) = p_a + 6\eta v_0 \int_{-\infty}^{x} dx' \left(\frac{1}{\bar{u}^2(x')} - \frac{u^*}{\bar{u}^3(x')}\right), \tag{B.1}$$

which we integrate until $p_{fluid}(x)$ vanish, which will happen for some value $x = x_1$ of the x coordinate. Next we replace u^* with $\bar{u}(x_1)$. We introduce the renormalized contact pressure $p_{cont}^{new} = \kappa p_{cont}$ and choose κ so that the pressure

$$p_0 = p_{cont}^{new} + p_{fluid}, \tag{B.2}$$

when integrated over x gives the loading force per unit length F_N/L. This gives

$$\kappa = \frac{F_N/L - \int_{-\infty}^{x_1} dx'\, p_{fluid}(x')}{\int_{-\infty}^{x_1} dx'\, p_{cont}(x')}. \tag{B.3}$$

Note from (7) it follows that $\bar{u}(0) = u_0$ and using (4) this gives

$$u_0 = \frac{h_{rms}}{\alpha}\ln\left(\frac{\beta E^*}{p_{cont}^{new}}\right). \tag{B.4}$$

We can write $\bar{u} = u_0 + w$ where

$$w(x) = \frac{x^2}{2R} - \frac{2}{\pi E^*}\int_{-\infty}^{\infty} dx'\, p_0(x')\ln\left|\frac{x - x'}{x'}\right|. \tag{B.5}$$

Finally, we calculate the new contact pressure

$$p_{cont} = \beta E^* \exp\left(-\alpha\frac{\bar{u}(x)}{h_{rms}}\right). \tag{B.6}$$

Return to start

If Δv is small enough, as the procedure outlined above is iterated n times it will give the properties of the system as the sliding velocity increases from zero up to $n\Delta v$.

Appendix C

Consider first a sliding junction where the sliding object has a flat surface tilted relative to the flat countersurface so the gap separating the solids has the height u_0 at the fluid exit and the height $u_1 > u_0$ at the fluid inlet. Neglecting fluid side-leak (which anyway is absent for the cylinder geometry studied in section 2), the average fluid pressure acting on the sliding solid is

$$p_{fluid} \approx p_a + \kappa\eta v_0 \frac{\lambda}{\bar{u}^2} \tag{C.1}$$

where p_a is the fluid pressure outside the sliding junction, $\bar{u} = (u_0 + u_1)/2$ is the average separation and κ is a number which only depends on $\xi = u_1/u_0$ (see, e.g., [12]):

$$\kappa = \frac{3}{2}\left(\frac{\xi + 1}{\xi - 1}\right)^2\left[\ln\xi - 2\frac{\xi - 1}{\xi + 1}\right].$$

If we assume that $(\xi - 1)/(\xi + 1) \ll 1$ we have $\kappa \approx 0.5(\xi - 1)$. From the simulations in section 2 we obtain $\xi \approx 1.4$ for all velocities where the fluid pressure is non-negligible (figures 5–7). This gives $\kappa \approx 0.2$. Using this we can calculate the average fluid film thickness from (C1), which is in good agreement with the values obtained from figures 5–7, and also with experiment [27]. In fact, Martin *et al* [27] have given a simple but crude argument for why κ should be at least approximately constant, independent of the details of the system under consideration.

Appendix D

Equations (23)–(27) are solved (numerically) with two different approaches depending on the lubrication regime, i.e. on the prevalence of hydrodynamic-driven phenomena or dry contact-driven phenomena. We denote the algorithm for boundary lubrication as BLP, and the algorithm for mixed and hydrodynamic lubrication by MHLS. The computational domain is a rectangular area and we use a constant grid size. The x direction is along the sliding direction. Both the numerical approaches require the discretization of the elastic integral (26)

$$\bar{u}_{ij} = u_0 + f_{ij} + \sum_{hk} \left(D^{hk}_{ij} - D^{hk}_{00}\right) \left[p_0\right]_{hk}, \qquad \text{(D.1)}$$

where $\bar{u}_{ij}$ is the separation at the grid point (i, j), u_0 is the central separation, f_{ij} is the undeformed shape of the contact and D^{hk}_{ij} is the discrete elastic kernel, with the translational invariance and symmetry property $D^{hk}_{ij} = D^{h-\mathrm{i},k-j}_{00} = D^{|h-\mathrm{i}|,|k-j|}_{00}$ (note: D^{hk}_{ij} can be obtained from the classical Love constant-square-pressure solution for the elastic half space). $[p_0]_{hk}$ is the zero-order expansion of the pressure field in the point (h, k). We use the convergence criteria:

$$N^{1/2} \frac{\sqrt{\sum_{ij} \left(s^n_{ij} - s^{n-1}_{ij}\right)^2}}{\sum_{ij} \left|s^{n-1}_{ij}\right|} < \varepsilon_s$$

where s^n_{ij} is $\bar{u}^n_{ij}$ or $[p^n_{\mathrm{c}}]_{ij}$ or $[p^n_{\mathrm{f}}]_{ij}$ (in this appendix we denote p_{fluid} as p_{f} and p_{cont} as p_{c}). In the present work we do not study starvation effects [29] because it does not change the basic phenomenon.

BLP for boundary lubrication

In the boundary regime, the effect of the fluid on the contact behavior is almost negligible. Thus, the solution of the dry contact problem will dominate the solution of the complete problem. In this case, the main algorithm loop is shown in figure D.1.

The BLP is an iterative contact solver (m-index loop) connected to a successive under-relaxation (SUR) process for the numerical convergence error dumping. To initialize the calculation, a Hertzian contact pressure or a solution from a different velocity run can be used. In each iteration, the fluid solver updates the fluid pressure with the actual approximation

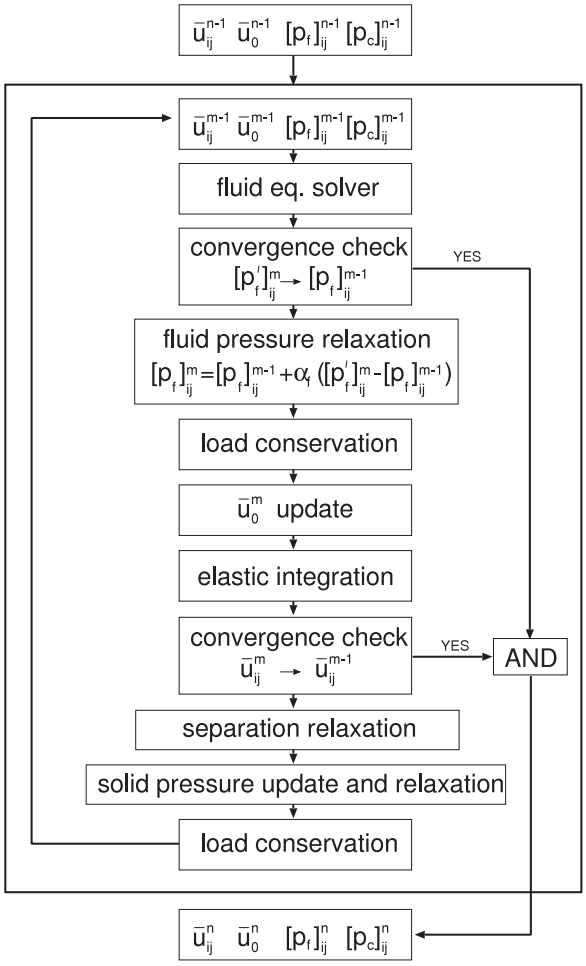

Figure D.1. BLP main loop.

$[p'_{\mathrm{f}}]^m_{ij}$ from the previous separation $\bar{u}^{m-1}_{ij}$. After a convergence check and under-relaxation of the fluid pressure (with α_f in the range $= 10^{-1}$ to 10^{-3}, the higher for smaller roughness), the load conservation is applied by rescaling fluid and solid pressure and updating the central separation, as described in appendix B for the line contact case. With the scaled pressure fields, the elastic integral is performed, followed by a convergence error check and under-relaxation of the actual separation approximation (with α_u in the range $= 10^{-1}$ to 10^{-3}, the higher for smaller roughness). Finally, from the relaxed separation, the solid pressure is updated and under-relaxed ($\alpha_c = 0.5$) and the load conservation is performed again by scaling the pressure fields. In our calculations, a convergence separation error of 10^{-5} and a convergence fluid pressure error of 10^{-4} was used.

The fluid solver (the l-index loop, inside the m-index loop) is an iterative solver based on the finite difference method to discretize (25) by mean of central second-order difference for both sides of the equality. The error relaxation is achieved by Gauss–Seidel (GS) sweeps along the x direction:

$$E_{ij}\left[p'_{\mathrm{f}}\right]^l_{ij} = -\big(A_{ij}\left[p'_{\mathrm{f}}\right]^l_{i-1,j} + B_{ij}[p_f]^{l-1}_{i+1,j} + C_{ij}\left[p_f\right]^{l-1}_{i,j-1} + D_{ij}[p_f]^{l-1}_{i,j+1}\big) + L_{ij}$$

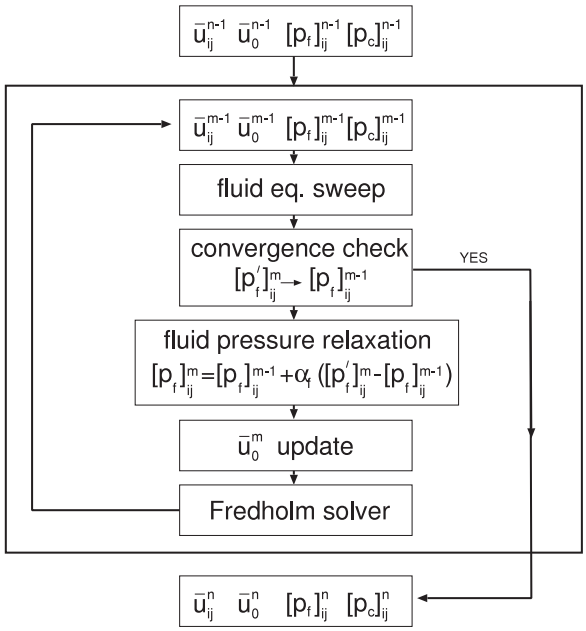

Figure D.2. MHLS main loop.

if $[p'_f]^l_{ij} > 0$ and $[p'_f]^l_{ij} = 0$ if $[p'_f]^l_{ij} < 0$. Here $[p_f]^{l-1=0}_{ij} = [p_f]^{m-1}_{ij}$. For SUR

$$[p_f]^l_{ij} = [p_f]^{l-1}_{ij} + \alpha\left([p'_f]^l_{ij} - [p_f]^{l-1}_{ij}\right)$$

where α is generally in the range 0.6–0.8. The l-index loop is stopped after reaching a convergence error of 10^{-7}. The calculation of frictional fluid stress is trivial. For the asperity–asperity interaction numerical approach, see [18].

MHLS for mixed and hydrodynamic lubrication

In the mixed and hydrodynamic regimes the asperity contact plays a minor role because of the increased separation due to the higher fluid pressure. In this case the BLP algorithm is not able to relax the residuals and the BLP procedure starts to diverge as soon as the fluid pressure becomes of the same order as solid pressure. This is a consequence of the nonlinear coupling between the fluid pressure and the separation in the Reynolds equation, which is not adequately handled in the BLP method. We now describe the MHLS algorithm (see figure D.2) which is able to handle this situation.

The algorithm is an iterative solver of the Reynolds equation coupled with the asperity interaction problem reformulated as a Fredholm problem. For the mixed and hydrodynamic range, the complete problem solution is driven (or dominated) by the fluid equation. For large separation (hydrodynamic range), the MHLS becomes simply an elastohydrodynamic lubrication (EHL) solver. The algorithm requires input solution fields (e.g. from a previously obtained BLP solution, or simply using a Hertzian-like fluid pressure) in order to initialize the system. The relevant features are the Reynolds sweep algorithm (RSA), the central separation updater (CSU) and the Fredholm solver (FS).

The RSA updates the fluid pressure solution by one-sweep-relaxing of the residuals of the Reynolds equation. By considering the general m iteration, the residuals of the fluid equation take the form

$$\begin{aligned} L^m_{ij} = {} & f_{i+1,j} - f_{i-1,j} + \sum_{hk}(D^{hk}_{i+1,j} - D^{hk}_{i-1,j})([p_f]^m \\ & + [p_c]^m)_{hk} - [A^m_{ij}[p_f]^m_{i-1,j} + B^m_{ij}[p_f]^m_{i+1,j} \\ & + C^m_{ij}[p_f]^m_{i,j-1} + D^m_{ij}[p_f]^m_{i,j+1} + E^m_{ij}[p_f]^m_{i,j}], \end{aligned} \tag{D.2}$$

where (25) was discretized by mean of second-order central difference scheme for both sides of the equality. The coefficients of (D.2) are

$$A^m_{ij} = \left[\bar{u}^3\right]^m_{i-1/2,j}\frac{2}{\lambda\delta_x}, \qquad B^m_{ij} = \left[\bar{u}^3\right]^m_{i+1/2,j}\frac{2}{\lambda\delta_x}$$

$$C^m_{ij} = \left[\bar{u}^3\right]^m_{i,j-1/2}\frac{2}{\lambda\delta_x}\frac{\delta_x^2}{\delta_y^2}, \qquad D^m_{ij} = \left[\bar{u}^3\right]^m_{i,j+1/2}\frac{2}{\lambda\delta_x}\frac{\delta_x^2}{\delta_y^2}$$

$$\begin{aligned} E^m_{ij} = -\frac{2}{\lambda\delta_x}\Bigg[& \left[\bar{u}^3\right]^m_{i-1/2,j} + \left[\bar{u}^3\right]^m_{i+1/2,j} \\ & + \frac{\delta_x^2}{\delta_y^2}\left(\left[\bar{u}^3\right]^m_{i,j-1/2} + \left[\bar{u}^3\right]^m_{i,j+1/2}\right)\Bigg] \end{aligned} \tag{D.3}$$

and implicitly depend on the fluid solution (through the Fredholm equation, see below). The fluid pressure is updated by a Newton–Raphson (NR) step:

$$\sum_{ab}\left[\frac{\partial L_{ij}}{\partial[p_f]_{ab}}\right]^{m-1}\left([p_f]^m - [p_f]^{m-1}\right)_{ab} = -L^{m-1}_{ij} \tag{D.4}$$

while if $[p_f]^m_{ab} < 0$ then $[p_f]^m_{ab} = 0$.

Observe that (D.4) cannot be solved with direct methods (a simple matrix inversion does not account for the cavitation condition, that is, it will solve a fluid equation that is not valid in all the domain). Depending on a third power, the coefficients (D.3) will vary on many scales into the computational domain; this suggests different behaviors of the fluid equation and so different degrees of coupling with the solid–solid interaction problem (a common numerical problem in the EHL community). For this reason, the domain is divided into three zones, namely a high fluid pressure zone C_1, a low pressure zone C_2 and a cavitation zone C_3.

Equation (D.4) is computationally simplified by considering the singularity of the elastic kernel:

$$\begin{aligned} -L^{m-1}_{ij} = {} & \left[\frac{\partial L_{ij}}{\partial[p_f]_{i-2,j}}\right]^{m-1}\left([p_f]^m - [p_f]^{m-1}\right)_{i-2,j} \\ & + \left[\frac{\partial L_{ij}}{\partial\left[p_f\right]_{i-1,j}}\right]^{m-1}\left([p_f]^m - \left[p_f\right]^{m-1}\right)_{i-1,j} \\ & + \left[\frac{\partial L_{ij}}{\partial[p_f]_{i+2,j}}\right]^{m-1}\left([p_f]^m - [p_f]^{m-1}\right)_{i+2,j} \\ & + \left[\frac{\partial L_{ij}}{\partial\left[p_f\right]_{i+1,j}}\right]^{m-1}\left([p_f]^m - \left[p_f\right]^{m-1}\right)_{i+1,j} \\ & + \left[\frac{\partial L_{ij}}{\partial[p_f]_{i,j}}\right]^{m-1}\left([p_f]^m - [p_f]^{m-1}\right)_{i,j} \\ & (i,j) \in C_1, \end{aligned} \tag{D.5}$$

$$-L_{ij}^{m-1} = \left[\frac{\partial L_{ij}}{\partial [p_f]_{i-1,j}}\right]^{m-1} \left([p_f]^m - [p_f]^{m-1}\right)_{i-1,j} + \left[\frac{\partial L_{ij}}{\partial [p_f]_{i+1,j}}\right]^{m-1} \left([p_f]^m - [p_f]^{m-1}\right)_{i+1,j} + \left[\frac{\partial L_{ij}}{\partial [p_f]_{i,j}}\right]^{m-1} \left([p_f]^m - [p_f]^{m-1}\right)_{i,j} \quad (i,j) \in C_2, \tag{D.6}$$

$$-L_{ij}^{m-1} = \left[\frac{\partial L_{ij}}{\partial [p_f]_{i,j}}\right]^{m-1} \left([p_f]^m - [p_f]^{m-1}\right)_{i,j} \quad (i,j) \in C_3, \tag{D.7}$$

Equations (D.5)–(D.7) are solved for each x line with a direct method. Observe that the coefficient matrix for the C_1 is a pentadiagonal matrix, for C_2 it is a tridiagonal matrix and for C_3 it is a single-diagonal matrix. The C_i domains are accurately determined in order to avoid multi-connected computational areas, small areas and boundary discontinuities between C_i and C_j.

The residual derivatives are

$$\frac{\partial L_{ij}}{\partial [p_f]_{i-2,j}} \approx D_{i+1,j}^{i-2,j} - D_{i-1,j}^{i-2,j} + \sum_{hk} \frac{\partial \beta_{ij}^{hk}}{\partial [p_f]_{i-2,j}} [p_f]_{hk}$$

$$\frac{\partial L_{ij}}{\partial [p_f]_{i-1,j}} \approx D_{i+1,j}^{i-1,j} - D_{i-1,j}^{i-1,j} - A_{ij} + \sum_{hk} \frac{\partial \beta_{ij}^{hk}}{\partial [p_f]_{i-1,j}} [p_f]_{hk}$$

$$\frac{\partial L_{ij}}{\partial [p_f]_{i,j}} \approx -E_{ij} + \sum_{hk} \frac{\partial \beta_{ij}^{hk}}{\partial [p_f]_{i,j}} [p_f]_{hk}$$

$$\frac{\partial L_{ij}}{\partial [p_f]_{i+1,j}} \approx D_{i+1,j}^{i+1,j} - D_{i-1,j}^{i+1,j} - B_{ij} + \sum_{hk} \frac{\partial \beta_{ij}^{hk}}{\partial [p_f]_{i+1,j}} [p_f]_{hk}$$

$$\frac{\partial L_{ij}}{\partial [p_f]_{i+2,j}} \approx D_{i+1,j}^{i+2,j} - D_{i-1,j}^{i+2,j} + \sum_{hk} \frac{\partial \beta_{ij}^{hk}}{\partial [p_f]_{i+2,j}} [p_f]_{hk}$$

$(h,k) = (i,j), (i-1,j), (i+1,j), (i,j-1), (i,j+1),$

where

$$-\sum_{hk} \frac{\partial \beta_{ij}^{hk}}{\partial [p_f]_{a,b}} [p_f]_{hk} \approx 3[\bar{u}^2]_{ij} \left(D_{i,j}^{a,b} - D_{0,0}^{a,b}\right) \times \left[\frac{[p_f]_{i-1,j} + [p_f]_{i+1,j}}{\lambda \delta_x} + \frac{\delta_x^2}{\delta_y^2} \frac{[p_f]_{i,j-1} + [p_f]_{i,j+1}}{\lambda \delta_x} - 2\left(1 + \frac{\delta_x^2}{\delta_y^2}\right) \frac{[p_f]_{i,j}}{\lambda \delta_x}\right]$$
$$+ 3[\bar{u}^2]_{i-1,j} \left(D_{i-1,j}^{a,b} - D_{0,0}^{a,b}\right) \frac{[p_f]_{i-1,j} - [p_f]_{i,j}}{\lambda \delta_x}$$
$$+ 3[\bar{u}^2]_{i+1,j} \left(D_{i+1,j}^{a,b} - D_{0,0}^{a,b}\right) \frac{[p_f]_{i+1,j} - [p_f]_{i,j}}{\lambda \delta_x}$$
$$+ 3[\bar{u}^2]_{i,j-1} \left(D_{i,j-1}^{a,b} - D_{0,0}^{a,b}\right) \frac{\delta_x^2}{\delta_y^2} \frac{[p_f]_{i,j-1} - [p_f]_{i,j}}{\lambda \delta_x}$$
$$+ 3[\bar{u}^2]_{i,j+1} \left(D_{i,j+1}^{a,b} - D_{0,0}^{a,b}\right) \frac{\delta_x^2}{\delta_y^2} \frac{[p_f]_{i,j+1} - [p_f]_{i,j}}{\lambda \delta_x},$$

where it is implicitly understood that the latter has to be determined at each m iteration. A SUR is applied at the end of the relaxation sweep, with a relaxation factor of order 0.1.

The CSU updates the central separation

$$\Delta \bar{u}_0^m = -\alpha_c \Delta F^m \qquad \text{if } \Delta F_c^m \cdot \Delta F^m \geqslant 0$$
$$\Delta \bar{u}_0^m = 0 \text{ otherwise}$$
$$\Delta F^m = \left[F_N - \delta_x \delta_y \left([p_f]^m + [p_c]^m\right)_{ij}\right]$$
$$\Delta F_c^m = \sum_{ij} \left([p_f]^m + [p_c]^m\right)_{ij} - \sum_{ij} \left([p_f]^{m-1} + [p_c]^{m-1}\right)_{ij}, \tag{D.8}$$

where α_c is in the range 10^{-2} to 1 (e.g. α_c can be put equal to $\bar{u}_0^{n-1}/F_N$ when starting from a previous velocity step solution). Equation (D.8), without the logical condition, is widely used by the EHL community to close the system of equations. Nevertheless, (D.8) cannot be obtained from equations (23)–(27). However, (D.8) can be understood as a Taylor expansion to the first order in the numerical step space with an average step size of α_c. This can obviously be a good average step size *only* if the error convergence history for the load conservation relation decreases exponentially. In our calculation the convergence history never has a monotonic form and (D.8) does not give the correct step size. The inequality condition introduces a *logical damping* into the convergence history of the contact solutions. The main idea is to update $\bar{u}_0$ *only if* a divergent behavior is otherwise observed for the total load.

After the update of the central separation, the shape of the contact is determined by solving the coupled elastic and solid contact equations as a Fredholm type of integral equation. The FS solves the latter by an NR method. Considering that $\bar{u}_{ij} > 0$, (D.1) can be rewritten as

$$0 = g_{ij} = -1 + \frac{\bar{u}_0 + f_{ij} + \sum_{hk} \left(D_{ij}^{hk} - D_{00}^{hk}\right) \left[p_f + p_c(\bar{u})\right]_{hk}}{\bar{u}_{ij}}. \tag{D.9}$$

By considering the form of the elastic kernel, the Jacobian **J** can be approximated

$$[\mathbf{J}]_{ij}^{lm} \approx \delta_i^l \delta_j^m \frac{\partial g_{ij}}{\partial \bar{u}_{lm}}$$

and so

$$\bar{u}_{ij}^l = \bar{u}_{ij}^{l-1} \left[1 + \alpha_{fs} \frac{g_{ij}^{l-1}}{1 + g_{ij}^{l-1} - \left(D_{ij}^{ij} - D_{00}^{ij}\right) \left[\frac{\partial p_c}{\partial \bar{u}}\right]_{\bar{u}_{ij}^{l-1}}}\right] \quad (i,j) \neq (0,0)$$

where α_{fs} is generally between 0.1 to 1 (the higher value for the hydrodynamic region, where $g_{ij}^n \to 0$). In our calculations, a target convergence error for fluid pressure field is 5×10^{-7}, with an average g_{ij} of 10^{-6}. After the update of separation, the loop restarts from RSA.

In figures D.3 and D.4 we show, respectively, film thickness and fluid pressure in a comparison between our numerical results and those of de Vicente *et al* [29] (we have removed the asperity–asperity interaction). The agreement is good, the difference in the maximum pressure may be due to a finer mesh size and a higher convergence target in our

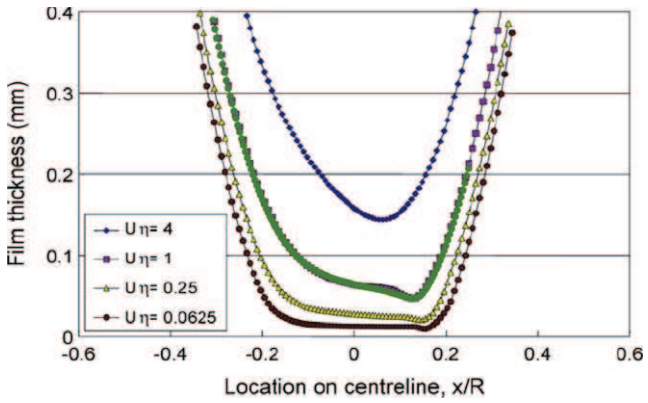

Figure D.3. Film thickness as obtained by de Vicente *et al* [29] compared with our results (green dots) for the following parameters: reduced elastic modulus $1/E^* = (1-\nu_a^2)/E_a + (1-\nu_b^2)/E_b$, $E^* = 5.45$ MPa, radius $R = 0.95$ cm, loading force $F_N = 3$ N, $U\eta = 1$. The computational range is $[-4a_H, 1.5a_H] \times [-3a_H, 3a_H]$ with 220×240 grid points.

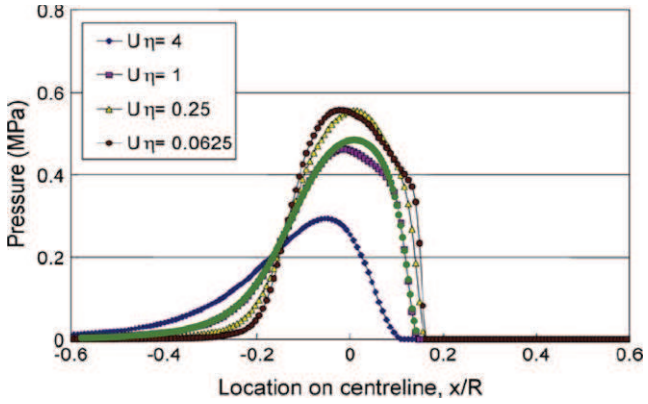

Figure D.4. Fluid pressure as obtained by de Vicente *et al* [29] compared with our results (green dots) for the same parameters of figure D.3.

calculation; in our results, the difference between the actual load F_{act} (numerical integration of pressure field) and the squeezing load F_N is $(F_{act} - F_N)/F_N = 5 \times 10^{-7}$. The mean residual of the fluid equation (to be considered with a pressure meaning), defined as $\frac{1}{N}\sum_{l_{ij}\neq 0} |\frac{l_{ij}-p_{ij}}{l_{ij}}|$, is 5×10^{-9} with a maximum residual value of 10^{-5}. The fluid pressure convergence error is lower than 5×10^{-10}.

References

[1] Dowson D 1998 *Meccanica* **33** 47
[2] Zhang C 2005 *Tribol. Int.* **38** 443
[3] Wang Q J and Zhu D 2005 *ASME J. Tribol.* **127** 722
[4] Zhu D, Martini A, Wang W, Hu Y, Lisowsky B and Wang Q J 2007 *ASME J. Tribol.* **129** 544
[5] Patir N and Cheng H S 1978 *ASME J. Lubrication Technol.* **100** 13
[6] Patir N and Cheng H S 1979 *ASME J. Lubrication Technol.* **101** 220
[7] Li W L 2000 *ASME J. Tribol.* **122** 869
[8] Harp S R and Salant R F 2001 *ASME J. Tribol.* **123** 134
[9] Sun D C 1978 *Proc. R. Soc.* A **364** 89
[10] Almqvist A and Dasht J 2006 *Tribol. Int.* **39** 994
[11] Sahlin F, Almqvist A, Larsson R and Glavatskih S 2007 *Tribol. Int.* **40** 1025
[12] Persson B N J 2000 *Sliding Friction: Physical Principles and Applications* 2nd edn (Heidelberg: Springer)
[13] Persson B N J and Mugele F 2004 *J. Phys.: Condens. Matter* **16** R295
[14] Martin P and Brochard-Wyart F 1998 *Phys. Rev. Lett.* **80** 3296
[15] Persson B N J, Volokitin A and Tosatti E 2003 *Eur. Phys. J.* E **11** 409
[16] Lebeck A O 1987 *J. Tribol.* **109** 189
[17] Lebeck A O 1987 *J. Tribol.* **109** 196
[18] Persson B N J 2001 *J. Chem. Phys.* **115** 3840
[19] Persson B N J 2007 *Phys. Rev. Lett.* **99** 125502
[20] Persson B N J 2006 *Surf. Sci. Rep.* **61** 201
[21] Persson B N J 2002 *Eur. Phys. J.* E **8** 385
[22] Persson B N J, Bucher F and Chiaia B 2002 *Phys. Rev.* B **65** 184106
[23] Yang C and Persson B N J 2008 *J. Phys.: Condens. Matter* **20** 215214
[24] Yang C, Persson B N J, Israelachvili J and Rosenberg K J 2008 *Europhys. Lett.* **84** 46004
[25] Johnson K L 1985 *Contact Mechanics* (Cambridge: Cambridge University Press)
[26] Vorvolakos K and Chaudhury M K 2003 *Langmuir* **19** 6778
Casoli A, Brendle M, Schulz J, Philippe A and Reiter G 2001 *Langmuir* **17** 388
[27] Martin A, Clain J, Bauguin A and Brochard-Wyat F 2002 *Phys. Rev.* E **65** 031605
[28] Goodyear C E 2001 Adaptative numerical methods for elastohydrodynamic lubrication *PhD Thesis* University of Leeds
[29] de Vicente J, Stokes J R and Spikes H A 2005 *Tribol. Lett.* **20** 273
[30] See e.g. Persson B N J, Albohr O, Tartaglino U, Volokitin A I and Tosatti E 2005 *J. Phys.: Condens. Matter* **17** R1
[31] Israelachvili J N 1995 *Intermolecular and Surface Forces* (London: Academic)
[32] Bongaerts J H H, Fourtouni K and Stokes J R 2007 *Tribol. Int.* **40** 1531
[33] Persson B N J 2006 *J. Phys.: Condens. Matter* **18** 7789
[34] Becker T and Mugele F 2003 *Phys. Rev. Lett.* **91** 166104-1
Nandi S K 2006 *Phys. Rev.* B **74** 167401
[35] Koenen A and Sanon A 2007 *Tribol. Int.* **40** 1484
[36] Deleau F, Mazuyer D and Koenen A 2009 *Tribol. Int.* **42** 149
[37] Experimental study by the Opel car company (unpublished)
[38] Westerman P *et al* (Goodyear Tire Company), private communication
[39] Persson B N J 2009 at press
[40] Persson B N J, Tartaglino U, Albohr O and Tosatti E 2005 *Phys. Rev.* B **71** 035428
[41] Greenwood J A and Williamson J B P 1966 *Proc. R. Soc.* A **295** 300
Bush A W, Gibson R D and Thomas T R 1975 *Wear* **35** 87
[42] Lorenz B and Persson B N J 2009 *J. Phys.: Condens. Matter* **21** 015003
[43] Mofidi M, Prakash B, Persson B N J and Albohr O 2008 *J. Phys.: Condens. Matter* **20** 085223
[44] Tominaga T, Takedomi N, Biederman H, Furukawa H, Osada Y and Gong J P 2008 *Soft Matter* **4** 1033
[45] Tominaga T, Kurokawa T, Furukawa H, Osada Y and Gong J P 2008 *Soft Matter* **4** 1645